

# Formation of 30 keV proton isotropic boundaries during geomagnetic storms

S. Dubyagin<sup>1</sup>, N. Yu. Ganushkina<sup>1,2</sup>, V. Sergeev<sup>3</sup>

<sup>1</sup>Finnish Meteorological Institute, Helsinki, Finland.

<sup>2</sup>Climate and Space Sciences and Engineering Department, University of Michigan, Ann Arbor, MI, USA.

<sup>3</sup>St. Petersburg State University, St. Petersburg, Russia.

## Key Points:

- Conditions at equatorial part of proton Isotropic Boundary field lines are analyzed using TS05 magnetospheric model and THEMIS observations
- Adiabaticity parameter values expected for isotropic boundary formation by scattering on curved field lines was found for 60%–80% of events
- Isotropic boundaries which do not fit this scenario reveal higher occurrence during the main phase or/and at latitudes lower than 59°

This is the author manuscript accepted for publication and has undergone full peer review but has not been through the copyediting, typesetting, pagination and proofreading process, which may lead to differences between this version and the [Version of Record](#). Please cite this article as doi: [10.1002/2017JA024587](https://doi.org/10.1002/2017JA024587)

Corresponding author: Stepan Dubyagin, [stepan.dubyagin@fmi.fi](mailto:stepan.dubyagin@fmi.fi)

## Abstract

We study the origin of the 30 keV proton Isotropic Boundary (IB) in the nightside auroral zone during geomagnetic storms, particularly, to address the recent results that the adiabaticity parameter  $K$  (ratio of the magnetic field line curvature radius to the particle gyroradius at the equator) on the IB field line can be much larger comparing to its theoretical estimate  $K \sim 8$  for the field line-curvature (FLC) scattering mechanism. During nine storms in 2011–2013, we investigate  $\sim 2000$  IBs observed by low-altitude POES satellites and apply the TS05 magnetospheric model to estimate the  $K$  value in the equatorial part of the IB field line. The statistical distribution of the estimated  $K$ -parameter, while being rather broad, is centered on  $K = 9$ –13. For smaller subset of  $\sim 250$  IBs, the concurrent magnetic field measurements onboard THEMIS probes in the equatorial magnetotail were used to correct the estimated  $K$ -values accounting for the TS05 deviations from the real magnetic configuration. After correction, the  $K$  distribution becomes narrower, being still centered on  $K = 9$ –12. Different estimates give percentages of events with  $K < 13$ , which can be attributed to IBs formed by FLC-scattering, between 60% and 80%. Finally, we have not found any dependence of the  $K$ -distribution on MLT and IB latitude, except for events with IB located at extremely low latitudes ( $< 59^\circ$ ). These findings imply that the FLC-scattering is a dominant mechanism of IB formation operating in a variety of magnetospheric conditions.

## 1 Introduction

The low-altitude observations of energetic particle fluxes always show the extended region of isotropic ion precipitation [e.g. *Imhof et al.*, 1977; *Søråas et al.*, 1977] which forms the proton auroral oval [*Donovan et al.*, 2003a]. The low-latitude edge of this region is called the isotropic boundary (IB). This isotropic precipitation reveals a strong pitch-angle diffusion, associated with violation of the first adiabatic invariant, which is capable to fill the loss-cone during one traversal across the current sheet [*Sergeev et al.*, 1983, 1993; *Ganushkina et al.*, 2005]. The IB delineates a boundary where the pitch-angle scattering suddenly becomes less effective when moving inward, to lower latitude in the ionosphere, where the fluxes in the loss-cone center become much lower than the fluxes of the locally trapped particles. The most frequently debated mechanisms of strong pitch-angle scattering responsible for isotropic proton precipitation on the nightside include the field-line-curvature-related (FLC) scattering [e.g., *Sergeev et al.*, 1983, 1993] and the scat-

46 tering by electromagnetic ion cyclotron (EMIC) waves [e.g., *Kennel and Petschek*, 1966;  
47 *Erlandson and Ukhorskiy*, 2001; *Liang et al.*, 2014]

48 A distinguishing feature of the FLC mechanism is that it is a very robust and much  
49 better understood in comparison to wave-particle interaction process. The amplitude of  
50 pitch-angle scattering depends on the ratio  $R_C/\rho$  where  $R_C$  is the magnetic field line  
51 curvature radius and  $\rho$  is the particle gyroradius in the current sheet center. It is beyond  
52 question that for  $R_C/\rho \ll 10$ , the adiabatic regime is severely violated and particle trajec-  
53 tories become chaotic in one particle current sheet crossing [*Büchner and Zelenyi*, 1989].  
54 This condition is fulfilled in the vast space of the tail plasma sheet outside  $r \sim 12\text{--}15R_E$ ,  
55 naturally providing isotropic proton distributions in the plasma sheet [*Wang et al.*, 2013],  
56 as well as extended isotropic precipitation in the proton auroral oval [*Donovan et al.*, 2003a].  
57 However, which particular mechanism is responsible for the proton precipitation in vicinity  
58 of the proton isotropy boundary is still under the discussion.

59 Analyses of charged particle trajectories in the simplified magnetic field models of  
60 the magnetotail current sheet [e.g., *Sergeev et al.*, 1983; *Delcourt et al.*, 1996] have shown  
61 that the condition for the complete loss-cone filling by FLC-scattering is  $K = R_C/\rho \leq 8$ .  
62 This equation can be rewritten as:

$$63 \frac{R_C}{\rho} \approx \frac{eB_Z^2}{mVdB_r/dZ} = \frac{eB_Z^2}{\sqrt{2mE}dB_r/dZ} \leq 8 \quad (1)$$

64  
65 Here,  $B_Z$ ,  $B_r$  are the magnetic field Z- and radial components,  $m$ ,  $V$ ,  $E$  are the par-  
66 ticle mass, velocity, and energy, respectively. According to the relation 1, if the FLC-  
67 scattering mechanism is responsible for the isotropy boundary formation, the IB location  
68 should strongly depend on the  $B_Z$  value in the conjugate current sheet. This prediction  
69 has a strong observational support [e.g., *Sergeev et al.*, 1993; *Donovan et al.*, 2003b], it  
70 can be used for remote sensing of the magnetotail magnetic configuration. Another pre-  
71 diction of the FLC-scattering mechanism is that, for a typical magnetotail configuration  
72 with equatorial  $B_Z$  increasing monotonically toward the Earth, the IBs for low energy par-  
73 ticles has to be observed poleward from the IBs for high energy particles. Such energy  
74 dispersion, indeed, is predominantly seen in the nightside observations [*Imhof et al.*, 1979;  
75 *Sergeev et al.*, 2015a]. The inverse order of energy dispersion (called as “anomalous” dis-  
76 persion) which is usually attributed to the wave-particle interaction process, can also be

77 sometimes observed [Donovan *et al.*, 2003b; Liang *et al.*, 2014; Sergeev *et al.*, 2015a]. Un-  
78 like the FLC-scattering mechanism, the particle interaction with EMIC waves theoretically  
79 can produce both types of the IB dispersion [Liang *et al.*, 2014].

80 Different from FLC mechanism, the EMIC waves excitation and efficiency of the  
81 pitch-angle scattering by EMIC waves depend on many factors [Kennel and Petschek,  
82 1966; Usanova *et al.*, 2016]. Horne and Thorne [1993] showed theoretically that the plasma-  
83 pause is a preferred location of EMIC waves excitations. Although this result was not  
84 fully supported observationally [Fraser and Nguyen, 2001], some authors did find on  
85 many occasions that the ions were scattered into loss-cone by EMIC waves near the plasma-  
86 pause [e.g. Yahnin and Yahnina, 2007; Yuan *et al.*, 2012; Xiong *et al.*, 2016]. More gener-  
87 ally, the theory predicts that EMIC wave excitation is favored by the presence of the cold  
88 ion population in addition to the anisotropic hot one [Gary *et al.*, 1995] and that ion com-  
89 position also plays a role [Kozyra *et al.*, 1984]. Meanwhile, the ambient magnetic field  
90 magnitude is also an important factor because it defines a particle resonance energy [Ken-  
91 nel and Petschek, 1966; Liang *et al.*, 2014]. Taken together, being dependent on combi-  
92 nation of many different factors to provide the strong diffusion rate and isotropic precipi-  
93 tation, the wave-particle interaction is evaluated as much less probable (anyway, less fre-  
94 quent) player in isotropy boundary formation. This is supported by the fact that IBs are  
95 always observed at all MLTs and under any conditions, while the EMIC wave occurrence  
96 strongly depends on MLT and geomagnetic activity [Halford *et al.*, 2010; Usanova *et al.*,  
97 2012; Keika *et al.*, 2013].

98 For a long time since Sergeev *et al.* [1993], it was generally accepted that FLC-  
99 scattering is the main mechanism of IB formation during low and moderate geomagnetic  
100 activity. This was questioned by the results of a few recent studies. In one approach, the  
101 statistics of standard and anomalous energy dispersion types was investigated. At low en-  
102 ergies (1–20 keV), Liang *et al.* [2014] found numerous cases of the inverse proton energy  
103 dispersion and showed a couple of cases in which EMIC waves were directly observed  
104 in the equatorial magnetosphere in the sector where the inverse IB dispersion was iden-  
105 tified. At higher proton energies (30 to 80 keV, which are preferable for remote sensing  
106 purposes), the situation seems to be different. According to large statistics presented in  
107 Sergeev *et al.* [2015a] the inverse dispersion is rare ( $\sim 5\%$ ), however, near the isotropy  
108 boundary the precipitation was found to display a complicated structure in almost half of  
109 events, including coincident IBs in 30 and 80 keV proton energy channels, frequent mul-

110 tiple dropouts of precipitated-to-trapped flux ratio near the IB location, and observations  
111 of newly emerging isotropic precipitation equatorward of the previous IB, which are hard  
112 to explain with a simple FLC-based model. Uncertainty in the IB identification in such  
113 events may influence their interpretation, therefore a further study of this aspect is desired.

114 Another approach to this problem is to verify experimentally the scattering condi-  
115 tion (Equation 1), namely: evaluate magnetospheric conditions in the equatorial part of  
116 the magnetic field line on which the proton IB is observed, estimate the local  $K$ -value in  
117 that place, and compare this value to its theoretical prediction ( $K = 8$ ). Generally, one  
118 has to use some magnetic field model to compute the  $K$ -value and to preform mapping of  
119 the field line where the IB is observed. Various magnetospheric models have been used  
120 for this purpose, including the empirical models [e.g. *Ganushkina et al.*, 2005], the adap-  
121 tive empirical models [e.g. *Pulkkinen et al.*, 1992; *Kubyskhina et al.*, 1999; *Sergeev et al.*,  
122 2015b], and the MHD global magnetospheric simulations [*Gilson et al.*, 2012; *Ilie et al.*,  
123 2015]. Accuracy of the model in representing the actual configuration is of the largest  
124 importance in such comparisons, the validation of the model's accuracy is also the least  
125 elaborated part of that kind of research. In two most recent attempts, it was found that the  
126 estimated  $K$ -value distribution for 30 keV protons is shifted to much larger values com-  
127 pared to the theoretical  $K = 8$ . Median  $K$ -values were 20 and 33, correspondingly, for  
128 32 and 40 IB crossings considered in *Sergeev et al.* [2015b] and *Ilie et al.* [2015]. This  
129 may imply that isotropy boundaries could be formed significantly inward from the  $K = 8$   
130 magnetic shell, suggesting a possible need of complementary proton scattering mecha-  
131 nisms in those regions acting, at least, in a significant percentage of cases. There were  
132 big differences in the models used (adaptive model and global MHD model, in *Sergeev*  
133 *et al.* [2015b] and *Ilie et al.* [2015], accordingly), as well as in the model validation (error  
134 estimation) tools applied in these papers, which makes a direct comparison of their re-  
135 sults difficult. Anyway, the results of both studies can not be generalized because the IB-  
136 crossing datasets included a relatively small number of events and most of them occurred  
137 during quiet conditions.

138 An important aspect of the problem is the possible differences in the IB forma-  
139 tion between quiet and storm times. Few studies specially addressed the peculiarities of  
140 the IB formation during storm periods though some authors used the storm-time IBs in  
141 their studies assuming one or another mechanism of their formation [*Søraas et al.*, 2002;  
142 *Asikainen et al.*, 2010]. *Dubyagin et al.* [2013] analyzed the nightside IBs observed dur-

143 ing one storm event and found that the anomalous IB dispersion is mostly observed in  
144 the dusk sector (MLT 18–21) during the main phase of the storm. The statistical studies  
145 confirmed that the EMIC waves occurrence also peaks in the dusk sector during the main  
146 phase [Halford *et al.*, 2010; Usanova *et al.*, 2012]. However, these authors found that the  
147 EMIC waves occurrence rate is quite low, especially for the inner magnetosphere (being  
148 less than 10% for 1 h MLT by  $1R_E$  bin). Concerning the proton precipitation, Gvozde-  
149 vsky *et al.* [1997] found that during and after strong magnetospheric disturbances, a weak  
150 pitch-angle scattering (anisotropic precipitation) is seen equatorward from the IB. It might  
151 be speculated that for some events and/or in some regions, the wave-particle interaction  
152 can become so strong that the flux inside the loss-cone would approach its value outside  
153 it, so that isotropic precipitation formed by the FLC-scattering in the poleward part would  
154 merge with the isotropic precipitation caused by the wave-particle interaction process in  
155 the equatorial part. In such a case, the observed IB would be formed by such (yet unspec-  
156 ified) wave scattering mechanism. Also, Yahnin and Yahnina [2007] found that the source  
157 region of intense EMIC waves is often the localized region where the injected hot ions en-  
158 counter the plasmasphere. However, although the ion injections are stronger and penetrate  
159 deeper during the storm periods, the plasmasphere also shrinks inward. Taking all these  
160 into consideration, it is not immediately obvious that the wave-related mechanism of the  
161 IB formation dominates during the geomagnetic storm periods. These aspects also need  
162 further study.

163 Our study is aimed to advance the understanding of the pitch-angle scattering mech-  
164 anism leading to the IB formation, with proper inclusion of the storm-time periods. By  
165 analyzing the loss-cone filling rate behavior near the IB, we take into account the un-  
166 certainty in possible identification of the isotropy boundaries and its dependence on the  
167 storm activity. Like in Sergeev *et al.* [2015b] and [Ilie *et al.*, 2015], we use the magne-  
168 topheric model to evaluate the  $K$ -values in the magnetosphere and pay attention to the  
169 proper model validation, however we do it on the larger statistics (thousands against a  
170 few tens of events) to evaluate statistically the most probable value of  $K$ -parameter in our  
171 database.

172 Here we use the data of seven NOAA/POES low-orbital satellites to detect the isotropic  
173 boundaries near the midnight meridian during nine storm events. The brief description of  
174 data and instrumentation is presented in Section 2. The data selection procedures are de-  
175 scribed in Section 3.1. In Section 3.2 we investigate statistical properties of the IB dataset

176 and present concise analysis of outliers. In Section 3.3, we use the empirical models to  
177 estimate  $K$ -parameter on the IB field line. To control the model accuracy, we use the con-  
178 current measurements of the magnetic field in the equatorial magnetosphere onboard Time  
179 History of Events and Macroscale Interaction During Substorms (THEMIS) spacecraft lo-  
180 cated at  $R \leq 10R_E$ . The detailed analysis of a few representative events is presented in  
181 Section 3.4. The results are discussed and the conclusions are drawn in Sections 4 and 5,  
182 respectively.

## 183 2 Data and Instrumentation

184 The low-altitude measurements are obtained from Space Environment Monitor-2  
185 (SEM-2) [Evans and Greer, 2000] onboard NOAA/POES satellites. SEM-2 consists of  
186 two detectors: (1) Total Energy Detector (TED) which measures energy flux of thermal  
187 protons and electrons in the energy range 50 eV–20 keV (2) Medium Energy Proton and  
188 Electron Detector (MEPED) which measures flux of the energetic protons and electrons  
189 from two orthogonal directions in a few energy channels. We use only two proton energy  
190 channels designated as P1 and P2, with nominal low energy thresholds 30 and 80 keV, re-  
191 spectively. One MEPED proton telescope is oriented nearly along the local zenith and it  
192 is referred to as  $0^\circ$ -telescope because it measures precipitating particles with  $\sim 0^\circ$  pitch-  
193 angles when a satellite is at the auroral latitudes. Another telescope points in a perpen-  
194 dicular direction, nearly in opposite direction to satellite velocity, it is referred to as  $90^\circ$ -  
195 telescope and it mostly detects the flux of locally trapped particles. This configuration  
196 allows the determination of the boundary between isotropic and anisotropic precipitations  
197 which is the focus of this study. The TED and MEPED detectors have a time resolution  
198 of 2 seconds but the accumulation cycles of the  $0^\circ$  and  $90^\circ$  MEPED telescopes are off-  
199 set by 1 second. For purely meridional orbits, the 2-second period corresponds to satellite  
200 displacement of  $\sim 0.12^\circ$  in latitude. We use the data from seven NOAA/POES satellites:  
201 NOAA-15,16,17,18,19, METOP-01,02. The data of METOP-01 satellite were available  
202 since October 2012 and NOAA-17 was not operating after April 2013. The satellites are  
203 positioned using the altitude-adjusted corrected geomagnetic (AACGM) coordinates (lati-  
204 tude and MLT) [Baker and Wing, 1989], computed using numerical field line tracing. The  
205 coordinates were adjusted to the geocentric distance  $r = 1R_E$ .

206 Magnetospheric observations come from the flux gate magnetometers [Auster *et al.*,  
207 2008] onboard three innermost probes of Time History of Events and Macroscale Inter-

**Table 1.** List of storm events selected for the analysis.

Date/Time	min( SYM-H )
2011-05-27/16:00:00 2011-05-31/00:00:00	-94
2011-08-05/18:00:00 2011-08-08/00:00:00	-126
2012-04-23/03:00:00 2012-04-26/00:00:00	-125
2012-06-16/20:00:00 2012-06-20/00:00:00	-69
2012-07-14/18:00:00 2012-07-18/00:00:00	-123
2012-09-30/11:00:00 2012-10-03/00:00:00	-138
2012-10-08/00:00:00 2012-10-11/00:00:00	-116
2013-05-31/16:00:00 2013-06-03/00:00:00	-137
2013-06-27/14:00:00 2013-07-01/00:00:00	-111

208 action During Substorms (THEMIS) mission [*Angelopoulos, 2008*]. The spin-resolution  
 209 (~ 3 sec.) data were averaged over 1 minute.

### 210 3 Data Analysis

#### 211 3.1 Isotropic Boundary Selection

212 Since our study relies on the concurrent observations at low-altitudes and in the  
 213 equatorial magnetosphere, we selected nine storms during 2011–2013 when THEMIS  
 214 apogees were on the nightside. These storms are listed in Table 1. They are moderate  
 215 storms with peak SYM-H values around -100 nT. The 3–4 days long intervals include a  
 216 sudden commencement (if it took place), the main phase, and one or two days of the re-  
 217 recovery phase.

219 The isotropic boundaries were selected using a visual inspection of the data of the  
 220 lowest energy channel (P1) of the MEPED proton detector. A nominal low-energy thresh-  
 221 old of this channel is 30 keV but the real energy can be somewhat higher due to the de-  
 222 tector degradation (but always lower than the energy of P2 channel, see more details in  
 223 Appendix). In this study, we do not determine isotropic boundaries for P2 channel, and  
 224 hence we do not analyze the IB energy-latitude dispersion. For P1 channel, we select only  
 225 IBs within 21–03 h MLT. This limitation was imposed to concentrate on the region where

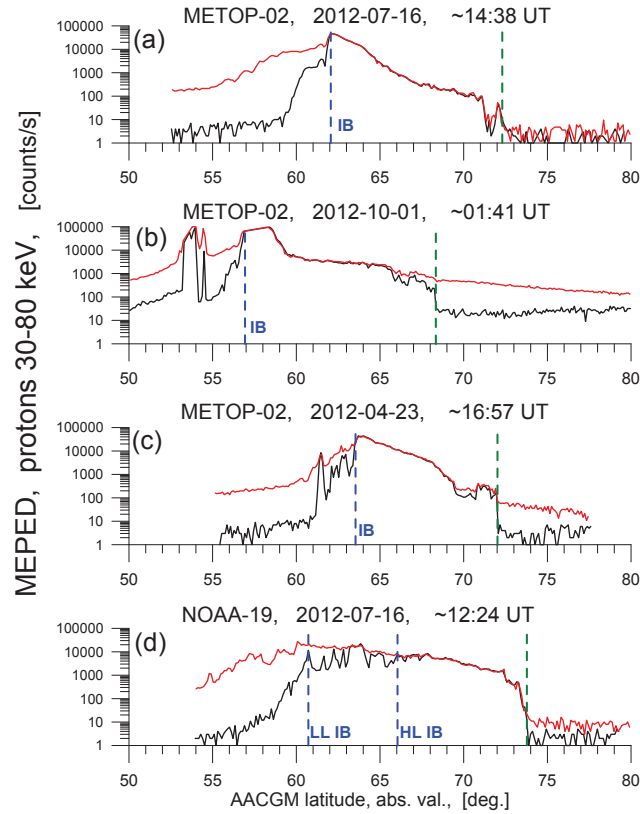


226

the empirical models are expected to be the most accurate (e.g. magnetotail twist effect in

227

presence of strong  $B_Y$  IMF is minimal).



228

**Figure 1.** Examples of proton flux latitudinal profiles. The black and red lines show precipitating and locally trapped fluxes, respectively. The green and blue dashed vertical lines mark the polar cap boundary and isotropic boundary, respectively. In the bottom panel, two dashed blue lines mark the low-latitude (LL) and high-latitude (HL) limits of the IB determination uncertainty interval.

229

230

231

232

Since the storm-time precipitations may have complicated structure, special caution should be taken when selecting IBs. Figure 1 shows four representative examples of the low-altitude proton flux observations during four different auroral region transits by METOP-02 and NOAA-19 satellites.

233

234

235

236

Figure 1a shows a typical latitudinal profile of the energetic proton fluxes. The isotropic precipitation from the plasma sheet is localized at lat.  $\sim 62\text{--}72^\circ$ . The low-latitude part (lat.  $\sim 50\text{--}60^\circ$ ) is occupied by strongly anisotropic fluxes: the fluxes of the locally trapped particles (red line) are  $> 2$  order of magnitude higher than the fluxes in the loss-cone (black line). There is a plateau-like region of the moderate anisotropy between these two

237

238

239

240

241 regions (lat.  $\sim 60\text{--}62^\circ$ ) which is supposedly caused by a wave-particle interaction process.  
242 The morphology and occurrence of such precipitation pattern were discussed by *Gvozde-*  
243 *vsky et al.* [1997]. The isotropic boundary can be unambiguously defined for this auroral  
244 region crossings at  $62.06^\circ$  (blue vertical line). The transition (marked by green vertical  
245 line) between substantial fluxes from the plasma sheet region and nearly zero fluxes from  
246 the polar cap region can be clearly discerned at  $72.3^\circ$ .

247 Figure 1b demonstrates a more complicated precipitation pattern. There is a local-  
248 ized region of the isotropic precipitations at  $\sim 53.5^\circ$  detached from the extended plasma  
249 sheet isotropic precipitations (lat.  $\sim 57\text{--}66^\circ$ ). Such localized low-latitude isotropic pre-  
250 cipitations are attributed to the wave-particle interaction process [*Yahnin and Yahnina,*  
251 *2007; Søråas et al., 2013a*]. IB was defined as an equatorial boundary of the plasma sheet  
252 isotropic precipitation at  $56.9^\circ$ . Note relatively high anisotropic fluxes in the polar cap for  
253 this event. These fluxes are likely resulted from the  $90^\circ$ -telescope contamination by the  
254 energetic neutral atoms from the ring current region [*Søråas and Sorbo, 2013b*], and the  
255 increased flux in the loss-cone was likely resulted from the solar proton event.

256 The pattern of the latitudinal profile in Figure 1c is somewhat similar to the previ-  
257 ous event. There is a localized isotropic precipitation at  $\sim 61.5^\circ$  detached from the bulk of  
258 the isotropic precipitations (lat.  $\sim 63.5\text{--}72^\circ$ ). However, for this event, the fluxes between  
259 these two regions are only slightly anisotropic (mostly  $< 1$  order of magnitude difference)  
260 and structured. An even more complicated pattern can be seen in Figure 1d. The wide  
261 region equatorward from the isotropic plasma sheet precipitations is occupied by alternat-  
262 ing isotropic/anisotropic fluxes (lat.  $\sim 62\text{--}67.5^\circ$ ). Such precipitation patterns are difficult  
263 to explain by either FLC-scattering or wave-particle interaction alone. In the former case,  
264 the radial profile of K-parameter should have quasi-periodic variations over an extended  
265 region. In the latter case, the intense waves in specific frequency range must be persis-  
266 tent over a wide range of radial distances which seems to be unrealistic given complexity  
267 and energy-selectivity of the criteria for wave-related pitch-angle scattering. On the other  
268 hand, we can not rule out the possibility that low- or mid-altitude processes can disturb  
269 isotropy of precipitating fluxes (though currently such mechanisms have not been sup-  
270 ported observationally). In these cases, the IB formed by FLC-scattering is projected to  
271 the low-latitude side of the region of alternating isotropy.

272 Given the uncertainty of the IB definition for such events, we opted to identify the  
273 upper and low bounds in latitudes which indicate the “uncertainty interval” of IB se-  
274 lection. These locations are referred to as LL (low-latitude) and HL (high-latitude) IBs.  
275 They are shown in Figure 1d as a blue dashed lines. The HL IB was defined as follow-  
276 ing: moving from the polar cap boundary to equator, we define HL IB as the last point of  
277 isotropic precipitation before the first occurrence of anisotropic precipitation. Note, how-  
278 ever, that we ignore the localized regions of anisotropy in the close vicinity of the polar  
279 cap boundary as it can be seen in Figure 1b (lat.~ 65.5–68.3°) and Figure 1c (lat.~ 69.5–  
280 70.5°). We also ignored single point deviations from isotropy as it can be seen in Fig-  
281 ure 1d (lat.~ 66.5 or ~ 67.5°). It should be mentioned that although, in general, polar  
282 cap is identified rather unambiguously as a region at high-latitudes with zero or small and  
283 constant flux level in all energy channels, it could not be observed for some orbits, e.g.  
284 for those skimming along the oval. In these cases, we started our algorithm from the point  
285 of highest latitude.

286 Unfortunately, it is hard to formulate strict formal criteria for LL IB. We tried the  
287 following criteria. First, it is located at a lower latitude than HL IB. Next, the fluxes be-  
288 tween HL and LL IBs should satisfy the following criteria:

- 289 1. The deviations from isotropy should be within a factor of 10.
- 290 2. There should be an alternation between isotropy and anisotropy (20% deviations  
291 from isotropy are considered as isotropic).
- 292 3. The LL IB is defined as the last point with less than factor 4 deviation from isotropy.

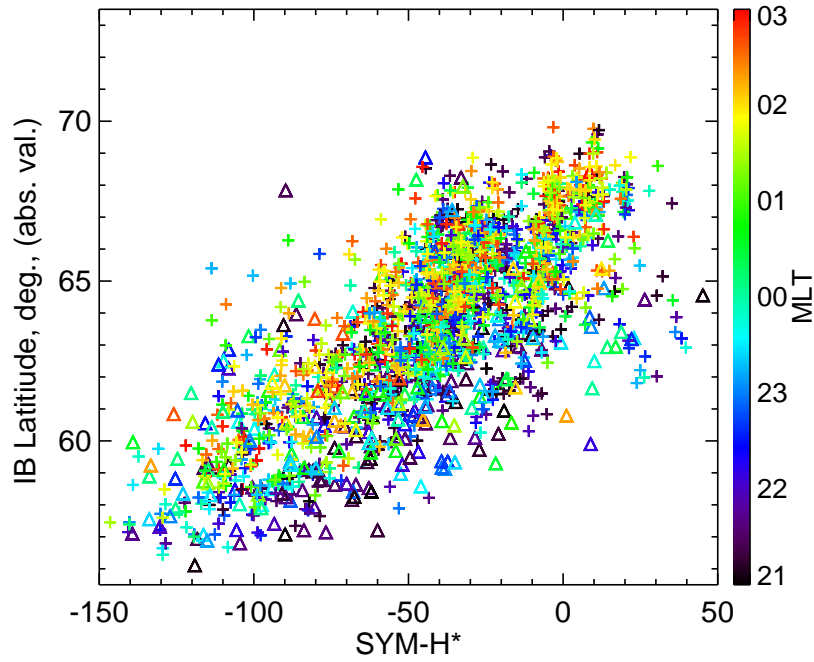
293 Even in an ideal case, IB can not be defined with accuracy better than  $0.12^\circ$  along the  
294 orbit ( $\sim 2$  sec. detector resolution). In addition, there is an uncertainty of calibration  
295 for degraded detectors. These factors were taken into account during selection HL and  
296 LL IBs for all crossings of the auroral region. Since the latitudinal difference less than  
297  $0.2^\circ$  can not be visually resolved in Figure 1, the IBs are shown as single lines in three  
298 top panels where an uncertainty of IB identification was very small. In total, 2277 pairs  
299 of HL and LL IBs have been selected. This dataset also includes the time intervals be-  
300 fore the storms. We deliberately extended the intervals in comparison to those in Table 1  
301 rounding the time of the storm beginning to the beginning of a day. These pre-storm  
302 events were included to investigate the IB evolution during a transition from pre-storm

303 to storm conditions. The number of events which are strictly inside the intervals specified  
304 in Table 1 is 1910.

### 305 3.2 Statistical Properties of Isotropic Boundary Data set

306 Having almost 2000 storm-time IBs selected, we start our analysis by exploring sta-  
307 tistical properties of this dataset. First, we investigated the response of the IB locations  
308 to a variation of the geomagnetic activity. Many authors noticed a good correlation be-  
309 tween the proton IB latitude and Dst index [*Hauge and Søråas, 1975; Søråas et al., 2002;*  
310 *Ganushkina et al., 2005; Lvova et al., 2005; Asikainen et al., 2010*]. Instead of Dst, we  
311 use here a pressure-corrected SYM-H index as it was proposed by *Burton et al. [1975]* :  
312  $\text{SYM-H}^* = \text{SYM-H} - 15.8\sqrt{P_{dyn}} + 20 \text{ nT}$ . This correction is needed because Dst and SYM-  
313 H indices include, apart from contributions from the ring and tail currents, also a con-  
314 tribution from the magnetopause current, which is controlled by dynamic pressure. The  
315 magnetopause currents affect the magnetic field in the dayside magnetosphere and on the  
316 ground (Dst and SYM-H) but its influence is much less prominent at the location of the  
317 IB formation. Thus, we subtract the magnetopause current contribution using *Burton et al.*  
318 [1975] equation.

321 Figure 2 shows the dependence of the IB AACGM latitude on SYM-H\* for LL IB  
322 dataset. For this figure, we only use data from those satellites for which the energy of  
323 P1 MEPED channel less than 50 keV (that is, with the detector revealing only moderate  
324 degradation, see Appendix ). The absolute value of latitude is shown to incorporate the  
325 observations from both hemispheres in one figure. Color corresponds to MLT of IB obser-  
326 vation (dark-blue is used for the pre-midnight sector and green-red for the post-midnight  
327 sector). We also computed the time derivative of the smoothed SYM-H\* index to analyze  
328 the relation with storm phases. To remove substorm-related short-scale variations and to  
329 smooth the original 1-minute resolution data, we use Fourier transform to filter out har-  
330 monics with periods shorter than 3 h. Triangles correspond to the SYM-H\* decrease pe-  
331 riods with  $d\text{SYM-H}^*/dt < -0.1 \text{ nT/min}$  (main phase) and crosses represent SYM-H\*  
332 increase or stagnation with  $d\text{SYM-H}^*/dt > -0.1 \text{ nT/min}$  (recovery and quiet periods). It  
333 can be seen that there are triangles in the region of positive SYM-H\* values. It should be  
334 noted that pressure-corrected SYM-H is supposed to be zero or negative, and that means  
335 that Burton's pressure correction has failed for these events. Our algorithm detected a  
336 drop of SYM-H\* caused by dynamic pressure drop, and marked these events as a main



319 **Figure 2.** Absolute value of proton IB AACGM latitude versus SYM-H\* for LL IB dataset. Triangles and  
 320 cross symbols correspond to main and recovery phases, respectively. Color shows IB MLT.

337 phase. However, further in the paper, these events can be easily identified in figures (e.g.  
 338 Figure 6) as we use color to show SYM-H\* value.

339 A few results are immediately obvious from Figure 2. First one is that IBs move  
 340 equatorward with SYM-H\* decrease. It also can be seen that the most equatorial IBs be-  
 341 long to the 21–24 MLT sector (blue color), indication a dawn-dusk asymmetry, and that  
 342 the low envelope of the data point cloud is formed by triangles, which correspond to the  
 343 strom main phase. Note, however, that triangles also form the upper envelop for SYM-  
 344 H < -75 nT. These outliers will be further investigated below. The figure in the same  
 345 format as Figure 2 but plotted for HL IB dataset (not shown), displayed only minor dif-  
 346 ference with Figure 2, demonstrating that, on average, the latitudinal difference between  
 347 HL and LL IBs is much smaller than the latitudinal data point scatter in Figure 2. The de-  
 348 tailed inspection showed that the difference between LL and HL IBs was > 0.2° for 29%,  
 349 > 0.5° for 15%, and it was as large as > 1° for 9% of events. We investigated the IB  
 350 uncertainty dependence both on the MLT and on the geomagnetic activity. No clear de-  
 351 pendence on MLT was found. However, the IBs with the uncertainty of > 1° were more

352 frequent during large negative SYM-H\*, that is during the main phase and near the peak  
 353 of the magnetic storm.

354 It can be seen that there are numerous outliers from the main cloud of points in Fig-  
 355 ure 2. Since such IBs can be presumably formed by different pitch-angle scattering mech-  
 356 anism, we investigate this sub-group separately. To identify these events, for both HL and  
 357 LL IB datasets we fitted the IB dependencies on SYM-H and  $P_{dyn}$  by following expres-  
 358 sion:

$$359 \Lambda_{IB} = G_0(MLT) + G_1(MLT) \cdot \text{SYM-H} + G_1(MLT) \cdot P_{dyn} \quad (2)$$

360  
 361 Here,  $\Lambda_{IB}$  is an absolute value of the IB latitude, and

$$362 G_i(MLT) = A_i + B_i \cdot \sin\left(\frac{MLT}{12h}\pi\right) + C_i \cdot \cos\left(\frac{MLT}{12h}\pi\right) \quad (3)$$

363  
 364 is the function of MLT.  $A_i$ ,  $B_i$ ,  $C_i$  are the free parameters (found using standard  
 365 least squared fit).

366 The goodness of the fit was evaluated using correlation coefficient (C.C.) and rms  
 367 deviation ( $\delta$ ) between the observed IBs and those predicted by Equation 2. The LL IB  
 368 dataset revealed higher fit quality (C.C.= 0.82 and  $\delta = 1.57^\circ$ ) as compared to the HL IB  
 369 dataset (C.C.= 0.76 and  $\delta = 1.83^\circ$ ). For this reason, we take LL IB dataset fit as our  
 370 reference model of the IB response to variation of the geomagnetic activity. Finally, we  
 371 selected those anomalous events when LL IBs were located at latitudes one  $\delta$  higher than  
 372 those predicted by our reference model (189 events).

373 Next, for these selected events, we investigate how the precipitated and trapped pro-  
 374 ton fluxes vary between and around the predicted and observed IBs. Specifically, how fast  
 375 the fluxes become anisotropic at latitudes lower than observed IB and whether there are  
 376 any specific features associated with the predicted IB location. To superpose latitudinal  
 377 profiles for all 189 anomalous events on a single axis, the normalized latitude ( $\Lambda^*$ ) was  
 378 computed for each event as following:

$$379 \Lambda^* = \frac{|\Lambda| - |\Lambda_{IB}^{observed}|}{|\Lambda_{IB}^{observed}| - |\Lambda_{IB}^{predicted}|} \quad (4)$$

380

381

382

383

384

Here,  $\Lambda$  is AACGM latitude for a particular event,  $\Lambda_{IB}^{observed}$  and  $\Lambda_{IB}^{predicted}$  are observed LL IB latitude and that predicted for this event using Equation 2. As a result of this coordinate transformation, the latitudes of observed and predicted IBs correspond to the points  $\Lambda^* = 0$  and  $\Lambda^* = -1$ , respectively.

387

388

389

390

391

392

393

394

395

396

397

398

For all 189 anomalous events, the percentiles of the precipitated-to-trapped flux ratio (ratio of fluxes measured by  $0^\circ$ - and  $90^\circ$ -MEPED P1 telescopes) were computed for a normalized latitude bin size of 0.1. Figure 3 shows these percentiles versus normalized latitude. The lines having color from dark-blue to red correspond to percentiles from 10% to 90% with 10% increment. It should be noted, that the fluxes can still be anisotropic at latitudes higher than observed LL IB ( $\Lambda^* = 0$ ) because moderate anisotropy is allowed between LL and HL IBs. Nevertheless, the precipitated-to-trapped flux ratio is very close to 1 in the  $\Lambda^* > 0$  region, indicating that the HL IB is located close to LL IB for a majority of selected events. On a negative side from  $\Lambda^* = 0$  point, all percentiles reveal a sharp drop by a factor 3–10 and stay at this level between  $\Lambda^* = 0$  and  $\Lambda^* = -1$  (that is, between observed IB and that predicted by Equation 2). At latitudes lower than predicted IB latitude, the precipitated-to-trapped flux ratio decreases by 1–2 order of magnitude.

399

400

401

402

403

404

405

406

407

We tried different selection criteria for the anomalous events to show that the drop of the precipitated-to-trapped flux ratio at  $\Lambda^*$  is not a coincidence. Only 28 events were found for stricter selection with  $|\Lambda_{IB}^{observed}| > |\Lambda_{IB}^{predicted}| + 2\delta$  but the aforementioned features were even more evident (the drop of the ratio at  $\Lambda^* = -1$  was steeper). Usage of the HL IB latitudes instead of  $\Lambda_{IB}^{observed}$  also led to the similar results. These results demonstrate that although Equation 2 fails to predict the IB location for these events, the predicted latitude corresponds to a special point where the pitch-angle distribution of precipitating protons makes a transition from slightly anisotropic on the poleward side to strongly anisotropic one, with almost totally depleted loss-cone, on its equatorial side.

408

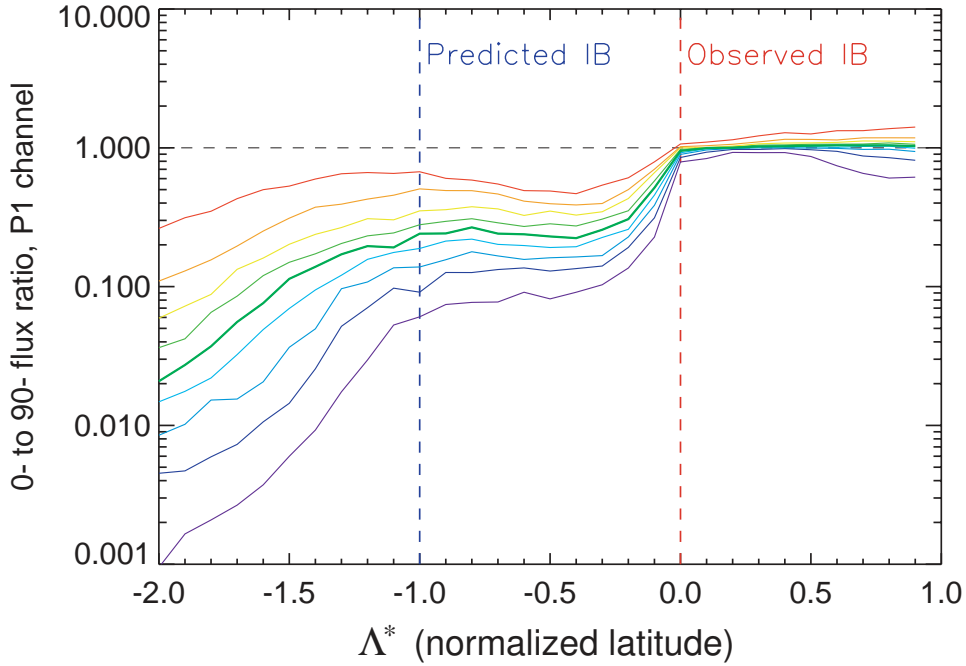
409

410

411

412

For these events, the latitudinal profiles of the  $0^\circ$ - and  $90^\circ$ -fluxes closely remind those of the specific events investigated by [Gvozdevsky *et al.*, 1997]. The authors argued that the extended region of the moderate anisotropy to the equator from IB is formed by wave-particle interaction. On the other hand, as an objection to this scenario, it should be mentioned that the intense wave-related scattering is believed to be spatially localized



385 **Figure 3.** Percentiles of the precipitated-to-trapped flux ratio versus normalized latitude for the subset of  
 386 anomalous events (see the text). 10% – 90% percentiles are shown with 10% increment.

413 (around plasmopause) but the regions of moderately anisotropic precipitations occupy a  
 414 broad range of latitudes in Figure 3 (larger than  $\delta = 1.57^\circ$ , owing to selection criteria).

### 415 3.3 *K*-parameter Estimation at the Isotropic Boundary

416 After surveying statistical properties of our IB dataset, we move to the main focus  
 417 of our paper: *K*-parameter estimation on IB field line. We use the empirical magneto-  
 418 spheric magnetic field model to trace a field line from the observed IB location at the  
 419 NOAA/POES orbit to the equatorial plane and to compute the *K*-parameter at the point  
 420 of the model magnetic field minimum. We use the *Tsyganenko and Sitnov* [2005] model  
 421 (hereafter TS05) which was specially designed to describe the storm-time magnetosphere.  
 422 The TS05 input parameters were available for 1841 event during the storm-time intervals  
 423 listed in Table 1.

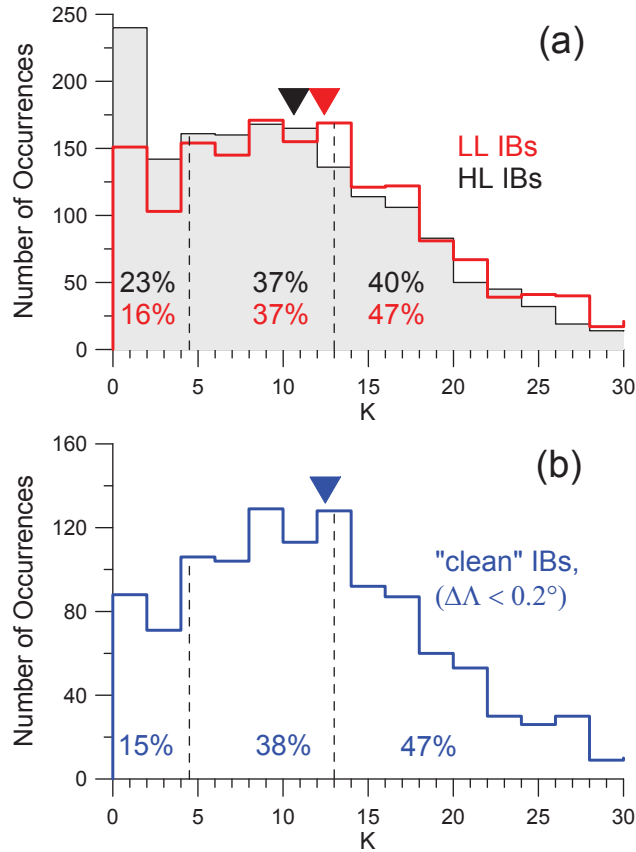
424 The model field lines were traced from both HL and LL IB locations to the equato-  
 425 rial plane where the curvature radius and gyroradius were estimated at the point of the  
 426 magnetic field minimum. The gyroradius was estimated for the particle energy corre-  
 427 sponding to the low energy limit of the P1 MEPED channel taking into account the cal-



428 ibration factors (See Appendix ). It should be noted that for 7% of HL IBs and for 3% of  
429 LL IBs, the traced field line went outside of  $r = 15R_E$  downtail, beyond TS05 model va-  
430 lidity limit, and  $K$ -parameter could not be estimated. Although it seems to be unrealistic  
431 and could be a result of wrong field line mapping (owing to the model inaccuracy), we  
432 do not discard these events because it would create a bias toward larger  $K$ -values in our  
433 statistics. Indeed, the model field lines traced from the IB location can as well go closer  
434 to the Earth than the real field line. In this case, the model's inaccuracy would not lead  
435 to such big error in terms of distance (due to the influence of the strong dipole field), but  
436 the error can be much larger in terms of  $K$  (due to stronger magnetic field gradient). For  
437 these reasons, we just assigned  $K = 0.1$  for all these events because  $K$ -values less than 1  
438 are expected in the distant tail [e.g. *Yue et al.*, 2014].

439 Figure 4a shows the histograms of estimated  $K$ -parameters for two datasets. Shaded  
440 black and red histograms represent HL and LL IB datasets, respectively. Figure 4b shows  
441 similar histogram but for a subset of events with the latitudinal difference between HL and  
442 LL IBs (uncertainty of IB determination) being within  $0.2^\circ$ , which will be referred to as  
443 “clean” IB dataset (1275 data records or  $\sim 70\%$  of the original dataset). The solid trian-  
444 gles mark the median values which were 10.7, 12.4, and 12.6 for HL, LL, and “clean”  
445 datasets, respectively. Although all three distributions were centered at  $K \approx 10$ –13, they  
446 are very broad. The increased number of occurrences in the first bin (especially for HL  
447 histogram) is due to the contribution of the events with  $K = 0.1$  assigned by hands if  
448 traced field line goes beyond  $r = 15R_E$  as discussed above. We also analyzed the depen-  
449 dence of the obtained  $K$ -parameters on MLT but found no clear trend.

454 When attempting to interpret Figure 4 in terms of pitch-angle scattering mecha-  
455 nism one has to take into account the following problems. First of all, the critical value of  
456  $K = 8$  was obtained by calculating particle trajectories in the idealized current sheet mag-  
457 netic field configurations (like those presented by TS05), and it should be considered as a  
458 rough estimate. Its actual value may change around this number depending on the differ-  
459 ent current distribution across the current sheet [*Delcourt et al.*, 2006], due to strong guide  
460 field ( $B_Y$ ) component [*Delcourt et al.*, 2000], because of enhanced radial  $B$ -gradients and  
461 other deviation from simplified magnetospheric models, which may be especially signifi-  
462 cant during magnetic storms. Second, there can be uncertainties in the IB determination  
463 of different kind, which should introduce a scatter of so-determined (mapped)  $K$ -values  
464 even if the model is perfect. Uncontrolled model deviations from reality and mapping er-

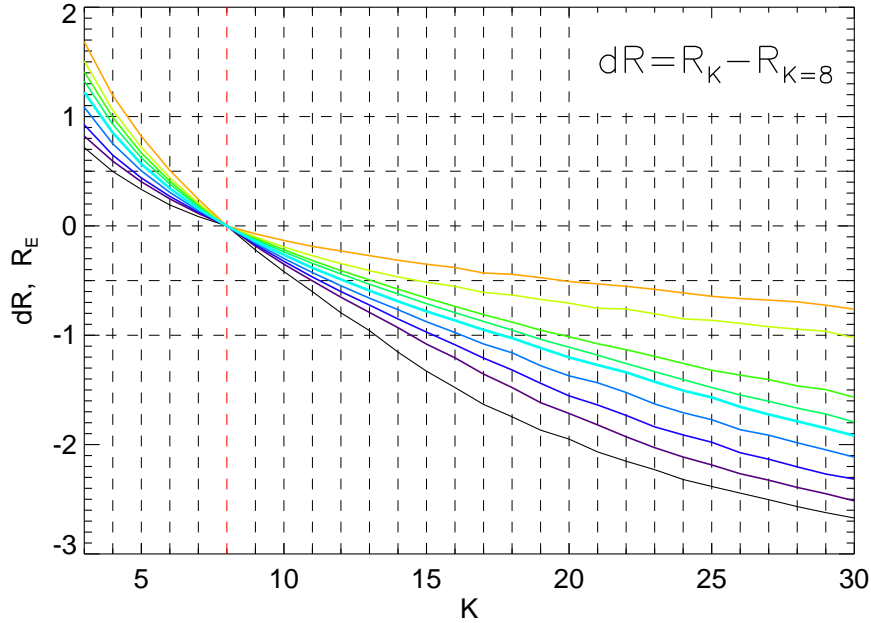


450 **Figure 4.** Histograms of  $K$ -parameter estimated for observed IB field lines using TS05. Panel (a): Shaded  
 451 gray and red colors correspond to HL and LL IBs, respectively. Panel (b): The same as panel (a) but for  
 452 “clean” IBs. Solid triangles mark the median values. The percentage shows the fraction of  $K$ -values in the  
 453 sectors separated by the black dashed lines.

455 errors also contribute to the scatter and are considered as a major source of errors. For un-  
 456 derstanding of how far the predicted equatorial IB location stays from the mapped one it  
 457 could be instructive to know how the deviations of the mapped  $K$ -parameter from  $K = 8$   
 458 correspond to the distance between their equatorial points, particularly, to learn which  $K$ -  
 459 range is associated with distance difference of, say,  $0.5-1R_E$ . This issue can be addressed  
 470 using the TS05 model.

474 We analyzed the radial profiles of the  $K$ -parameter in TS05 model. For HL IB dataset  
 475 we computed the  $K(r)$  profiles (at  $B$ -minimum) at the MLT meridians corresponding to  
 476 the IB observations. We emphasize that the choice of IB dataset plays no role here be-  
 477 cause IB latitude is not used. We only use the TS05 input parameters corresponding to

478 IB observation time (as a representation of storm-time external conditions) and IB MLTs  
 479 (just because they cover 21–03 MLT sector). For every profile, we defined  $dR(K) = r(K) -$   
 480  $r(K = 8)$ , where  $r(K)$  is a geocentric distance to the point with corresponding  $K$ -parameter.  
 481  $dR$  can be plotted as a function of  $K$ . Figure 5 shows statistical distribution of the  $dR(K)$ -  
 profiles for the events shown in Figure 4. The percentiles of  $dR$  were computed for all



471 **Figure 5.** Statistical relation between  $K$  and  $dR$  obtained using TS05. Here,  $dR$  is a distance between the  
 472 point with specific  $K$  (shown on the horizontal axis) and the point with  $K = 8$ . Percentiles of  $dR$  are shown  
 473 ranging from 10% to 90% with 10% increment.

482  
 483 TS05 model's  $K(r)$ -profiles for  $K$ -parameter bin size of 1. In Figure 5, the  $dR$ -percentiles  
 484 ranging from 10% to 90% with 10% increment are shown versus  $K$  as blue-to-red curves.  
 485 The black curve (lowest percentile) crosses  $dR = -1R_E$  (bottom horizontal dashed line)  
 486 line at  $K \approx 13$ . It means that the model's  $K = 13$  point is located within  $1 R_E$  from the  
 487 point with  $K = 8$  for 90% of the model's configurations. On the other hand, red curve  
 488 (highest percentile) crosses  $dR = +1R_E$  line at  $K \approx 4.5$  meaning that the point with  
 489  $K = 4.5$  is located within  $1 R_E$  from the point with  $K = 8$  for 90% of configurations.  
 490 In other words, the model's estimation of  $K$ -parameter between 4.5 and 13 corresponds  
 491 to field lines whose equatorial points cluster in a very narrow region, being within  $1 R_E$   
 492 from the model field line with  $K = 8$ . Since the accuracy of  $1 R_E$  is a quite optimistic

493 estimate for the ionosphere-magnetosphere mapping, the  $K$ -values within this range can be  
494 considered as supporting FLC-scattering mechanism of IB formation. If the allowed field  
495 line deviation from the line with  $K = 8$  is  $0.5R_E$ , the interval  $K = 6-10$  corresponds to  
496 90% of events fitting this stricter limit. It should be noted, that even for  $K = 30$ , two high-  
497 est percentiles in Figure 5 (red and yellow curves) are still higher than  $dR = -1R_E$  line,  
498 indicating that for  $\sim 20\%$  of events, the point with  $K = 30$  is located within  $1 R_E$  from  
499 the point with  $K = 8$ . These points obviously correspond to the configurations with a very  
500 strong radial gradient of the equatorial magnetic field.

501 Coming back to Figure 4, 37%, 37%, and 38% of events are inside  $K = 4.5-13$  in-  
502 terval for HL, LL, and “clean” IB data sets, respectively. Since we found that the points  
503 with  $K = 4.5-13$  are spatially very close (within  $1 R_E$ ) to  $K = 8$  point in the TS05 model  
504 (see Figure 5), this percentage can be considered as a rough estimate for the occurrence  
505 rate of IBs formed by FLC-scattering. However, we can not be sure that the  $K$ -values out-  
506 side this interval necessarily correspond to IBs formed by some other mechanism because  
507 there is no information on the actual model mapping accuracy for these events, which  
508 could be much worse than  $1R_E$ . Next step will be to evaluate the deviations of the model  
509 configuration from the real one and attempt to correct the mapped  $K$ -values.

510 Since the TS05 model is statistical in nature, its deviation from the real configu-  
511 ration for a particular event can be large, especially during dynamic storm events. For  
512 this reason, the independent control of the model accuracy is needed. To evaluate the  
513 model accuracy for a particular event, we compare the magnetic field measurements at the  
514 THEMIS probes with those predicted by the models. To control the model in the region  
515 of the expected IB projection, we selected those events in which the THEMIS probes were  
516 within  $r = 4-10R_E$  and within  $\pm 1$  h in MLT from observed IB. This selection reduced a  
517 number of IBs in our dataset to 244.

518 Which measurable parameters are suitable to control the model performance? The  
519 IB formation is controlled by  $B_Z^2/(dB_X/dz)$  (Equation 1). However, the deviation of the  
520 solar wind velocity from the radial direction can be as large as several degrees, and the  
521 current sheet can undergo strong large-scale flapping oscillations. It means that the model  
522 prediction of the current sheet position ( $Z$ -coordinate) and  $B_X$  can often be unreliable.  
523 On the other hand, for the thin current sheet (1D-like) configurations,  $B_Z$  is nearly con-  
524 stant across the current sheet. It means that, even if the model prediction of the current

525 sheet position is wrong, the model estimations of  $B_Z$  are less affected. Since the equato-  
 526 rial  $B_Z$  is the main parameter which controls the mapping and it enters Equation 1 as a  
 527 second-degree power exponent, we use the difference of the  $B_Z^{OBS}$  and  $B_Z^{MOD}$  as a proper  
 528 indicator of the model accuracy (GSM coordinates are used).

529 There were often 2 or 3 THEMIS probes in conjunction with IB ( $r = 4-10R_E, \pm 1$  h  
 530 from IB). In such cases, we use the average over all probes in the region:

$$531 \quad \Delta B_Z = \langle B_Z^{OBS} - B_Z^{MOD} \rangle = \frac{1}{N} \sum_{i=1, \dots, N} (B_{Zi}^{OBS} - B_{Zi}^{MOD}) \quad (5)$$

532  
 536 Figure 6 shows the TS05 model estimations of the mapped  $K$ -parameter against  
 537  $\Delta B_Z$  for HH (a), LL (b), and “clean” (c) IB datasets. The “clean” IB dataset supported by  
 538 THEMIS observation comprises only 169 events. Color corresponds to SYM-H\* as shown  
 539 on the right (positive SYM-H\* is shown by black). Triangle and cross symbols correspond  
 540 to the main and recovery phases as defined in Section 3.1. Negative  $\Delta B_Z$  corresponds to  
 541 the events when model  $B_Z$  is stronger than real  $B_Z$ , that is, the model overestimates  $K$ -  
 542 parameter (see Equation 1). In addition, it means that the model is understretched and  
 543 the equatorial projection of the IB field line is closer to the Earth than the real field line,  
 544 and again  $K$ -parameter is overestimated. The opposite is true for positive  $\Delta B_Z$ : the model  
 545 underestimates  $K$ -parameter for such events. The expected  $\Delta B_Z$  control is obvious in all  
 546 three panels of Figure 6, the clouds of points obviously have the negative slopes.

550 We selected those events in which the modeled and measured magnetic field agree  
 551 to within 5 nT and computed the median of  $K$ -parameter for the events. This region is  
 552 marked in Figure 6 by the red vertical dashed lines and the median  $K$  values are shown in  
 553 red font at the bottom of the panels. It can be seen that median values vary between 9.2–  
 554 10.6, being close to  $K = 8$  expected for the FLC-scattering mechanism. Figures 7a and 7b  
 555 show the histograms of the  $K$ -parameter for the events with  $|\Delta B_Z| < 5$ nT for the HL and  
 556 LL (panel a) and “clean” (panel b) IB datasets. If compared to Figure 4, the scatter of  $K$ -  
 557 values was reduced, with the percentage of events with  $K > 13$  changing from 40%–47%  
 558 in Figure 4 to 29%–34% in Figures 7a and 7b. We checked how the percentage of the  
 559 events with  $K < 13$  (which can be attributed to the FLC-scattering mechanism) depended  
 560 on the allowed model accuracy. For LL IB dataset, we found 64%, 68%, 76%, and 77%  
 561 for  $|\Delta B_Z|$  less than 10, 5, 2, and 1 nT, respectively. The number of events for these four

subsets was 138, 80, 37, and 22, respectively. This sequence is converging to  $\sim 80\%$  of the events with  $K < 13$  for  $\Delta B_Z = 0$ . The similar numbers were obtained for HL IBs, and “clean” IBs datasets (except for the fact that there are fewer events in the “clean” dataset).

However, it should be also noted that the majority of events in the region of the high model accuracy correspond to the periods of low and moderate disturbances (SYM-H\*  $> -40$  nT). In addition, the main phase is represented by eight points only and  $K > 13$  for five of them. On the other hand, there are more events corresponding to active storm periods in the region of large negative  $\Delta B_Z$ . Now we attempt to correct the  $K$ -distributions. Since the  $K$ -parameter values in Figure 6 demonstrate clear dependence on  $\Delta B_Z$ , we try to subtract this trend mathematically shifting  $K$ -values to the  $\Delta B_Z = 0$  line. We fit the points with  $|\Delta B_Z| < 20$  nT using a linear regression in log-linear scale:

$$\log K = C_1 + C_2 \cdot \Delta B_Z \quad (6)$$

$C_1$  and  $C_2$  are free parameters found using standard least-squares minimization. The resulting fits are shown in all panels of Figure 6 by black dashed line. Using the obtained  $C_2$  parameter, the  $K$  values can be corrected as:

$$K^* = K \cdot \exp(-C_2 \Delta B_Z) \quad (7)$$

Here and throughout the paper the asterisk symbol is used to differentiate the  $K$ -parameter corrected using Equation 7 ( $K^*$ ) from original uncorrected value ( $K$ ). Equation 7 essentially performs a projection of the points onto the  $\Delta B_Z = 0$  line along a direction parallel to the dashed line and this correction was applied to all  $K$ -values irrespective of  $\Delta B_Z$ . Note that correcting factor exponentially depends on  $\Delta B_Z$ , demonstrating a high sensitivity of the estimated  $K$ -parameter to the model error in  $B_Z$ . For example, the model’s  $B_Z$  error of 5 nT leads to  $\sim 30\%$  error of estimated  $K$ .

Figures 7c and 7d show the histograms of  $K^*$  in the same format as panels (a) and (b). It can be seen that the percentages of events for three selected intervals of  $K$ -parameter are quite similar to those obtained if only events with  $|\Delta B_Z| < 5$  nT are considered.  $K^* > 13$  was found for  $\sim 30\%$ – $40\%$  of events, the percentage is 10% lower than that in Figure 4. The difference is even more evident for higher  $K$ -values, the percentage of events with  $K > 20$  is almost twice lower ( $\sim 15\%$ ) in Figures 7c, d as compared to  $\sim 25\%$  in Figure 4. The difference is even more pronounced for events with  $K > 30$ , 5% and 14%

592 in Figures 7d and 4b, respectively. This means that considerable part of high  $K$  events in  
593 the uncorrected  $K$ -distributions are false numbers, caused by the understretched magnetic  
594 configuration in the model. At the same time, the distributions in Figures 7c and 7d still  
595 peak within  $K = 4.5\text{--}13$ , with median values of  $K^*$  being 9.2, 10.9, and 11.1 for HL, LL,  
596 and “clean” datasets, respectively.

599 Figure 8 shows the estimated  $K^*$ -values against the IB latitude for HL (top) and LL  
600 (bottom) IB datasets. Color corresponds to MLT. For IBs located at latitudes  $\sim 59\text{--}66^\circ$ ,  
601 the estimated  $K^*$ -values show no dependence on IB latitude. However, the  $K^*$ -values are  
602 systematically higher than 8 for IBs located lower than  $\sim 59^\circ$  and systematically lower  
603 than 8 for those located higher than  $\sim 66^\circ$ . This does not necessarily mean that IBs at lat-  
604 itudes lower than  $59^\circ$  are formed in the region of higher  $K$ . Indeed, the method which  
605 was used to correct for the model bias (Equation 7) is quite primitive and can fail for  
606 large  $\Delta B_Z$ . We did find that  $\Delta B_Z$  was greater than 10 nT for all IBs at latitudes lower  
607 than  $59^\circ$ . In addition,  $K^*$  is systematically lower for IBs located at high latitudes, indicat-  
608 ing that the model fails to describe these configurations (no other explanation can be de-  
609 vised for low  $K^*$  values). It can be speculated that the model is accurate for regular con-  
610 figurations with IB latitudes in  $\sim 60\text{--}66^\circ$  range, but it becomes biased for extreme events  
611 just as for IB latitudes lower than  $59^\circ$  so for IB latitudes higher than  $66^\circ$ . It is important  
612 that there is no clear dependence of  $K^*$ -parameter on MLT for these datasets, while this  
613 dependence is rather obvious in Figure 2 for IB latitude. We also plotted the histograms  
614 of  $K^*$  for different MLT sectors (not shown), but again, no distinct difference was found.  
615 It should be noted that this is exactly what expected for the FLC-scattering mechanism of  
616 IB formation:  $K \approx 8$  irrespective of where IB is projected to.

617 Finally, we inspected the  $K$  values for the high-latitude outliers events which were  
618 selected in Section 3.2. Unfortunately, there were no suitable THEMIS observations avail-  
619 able for the majority of these events and the correction of the  $K$  values could not be ap-  
620 plied. Since the results presented in Section 3.2 imply that the latitude predicted by Equa-  
621 tion 2 ( $\Lambda^* = -1$  in Figure 3) corresponds to the low-latitude boundary of some pitch-angle  
622 scattering mechanism, we also investigated the conditions in the equatorial region for these  
623 points as well as for observed IBs. The median  $K$  values of 4.5 and 19.3 were found for  
624 the observed and predicted IBs, respectively. For observed IBs,  $K$ -values within 4.5–13  
625 range was found in 42% of events. On the other hand, for predicted IBs, the fraction of  
626 such events was only 21%. That is, if the observed and predicted IBs are compared, these

627 are rather observed IBs which agree with the FLC-scattering mechanism of IB formation.  
628 The somewhat lower  $K$ -values for these events are likely caused by the mapping errors.

### 629 **3.4 Detailed Analysis of Selected Events**

631 To gain further insight about what causes the diversity of the  $K$ -values, we present  
632 a detailed analysis of a few selected events. Figures 7a and 7b show that for the events  
633 when the TS05 model is in a good agreement with magnetic field measurements the dis-  
634 tribution of  $K$ -parameter, though still broad, peaks at  $K \approx 9$ –11. However, for these  
635 events (region marked by vertical dashed lines in Figure 6), there are only 9–10 points  
636 (9 for HL and 10 for LL IB datasets) corresponding to the storm peak periods with  $\text{SYM-}$   
637  $H^* < -80$  nT and these points are scattered between  $K \approx 1$  and  $K \approx 30$  (not shown).  
638 Of these ten events, we selected those belonging to one of three groups according to their  
639  $K$ -value:  $K > 20$ ,  $6 < K < 10$ ,  $K < 3$ . The central  $K$ -interval corresponds to the  $K$ -  
640 values expected for FLC-scattering. The values of  $K = 6$  and 10 were chosen as those  
641 corresponding to the points located within  $0.5R_E$  from the point with  $K = 8$  (see Fig-  
642 ure 5). Two other  $K$ -intervals correspond to  $K$ -values which can not be easily explained  
643 using FLC-scattering mechanism. The IBs with  $K > 20$  can be hypothetically formed by  
644 the wave-particle interaction but we have not a plausible explanation for the events with  
645  $K < 3$  other than inaccurate model predictions. Luckily, the same events were selected  
646 for both LL and HL datasets. These events are listed in Table 2. All parameters corre-  
647 spond to LL IBs but those for HL IBs were very close. We analyze these events in details  
648 trying to figure out what is the difference between the evens with  $K$  expected for the FLC-  
649 scattering mechanism and other events. The columns of Table 2 are (from left to right):  
650 satellite name, IB observation time, the  $\text{SYM-H}$  index,  $K$ -parameter at the IB field line  
651 computed using TS05, the observed IB latitude, and the last column is explained later.  
652 We inspected all available observations during these events in an attempt to find the char-  
653 acteristics which would be discriminating between these three groups. However, nothing  
654 specific was found in THEMIS observations, model predictions, or shape of latitudinal  
655 profiles of the low-altitude fluxes except for one event which will be discussed later.

656 Figure 9 shows survey plots for the storms when IBs listed in Table 2 were ob-  
657 served. Each panel of Figure 9 shows the  $\text{SYM-H}^*$  index (magenta curve, the axis is on  
658 the right) with the overlapped latitudes of observed HL IBs (black crosses, the axis is on  
659 the left). LL IBs are shown by small red crosses if the difference in latitude with respect



**Table 2.** Selected events categorized according to the predicted  $K$ -parameter

Satellite	Date/Time	SYM-H*	$K$	IB Latitude	Color
NOAA-15	2013-06-29/06:16:24	-112	0.48	-63.43	blue
NOAA-17	2012-07-16/00:24:46	-100	2.4	-65.06	blue
NOAA-18	2012-04-24/02:31:45	-124	9.7	-59.44	red
NOAA-18	2012-07-15/17:52:06	-113	8.15	-60.00	red
NOAA-19	2013-06-01/11:10:25	-91	7.0	-62.37	red
NOAA-19	2013-06-01/13:58:47	-82	9.6	62.41	red
NOAA-17	2012-10-01/08:36:28	-96	23.9	-60.52	green
NOAA-19	2012-04-24/02:25:48	-123	28.8	-58.35	green

660 to HL IB was greater than  $0.5^\circ$ . IBs listed in Table 2 are shown by thick colored cross  
 661 symbols. Red, green, and blue colors correspond to  $6 < K < 10$  (expected for the FLC-  
 662 scattering),  $K > 20$  (possibly wave-particle interaction), and  $K < 3$  (wrong mapping or  
 663 some unknown mechanism of the pitch-angle distribution transformation), respectively.

667 It can be seen that the IB latitudes follow the variations of SYM-H\* closely except  
 668 for transient periods when the IB latitude shows up and down excursions (for example  
 669 2012-04-23/22:00–2012-04-24/02:00). A prominent difference between HL and LL IBs  
 670 can be seen during these IB excursions. Two IBs with  $K < 3$  (blue thick cross symbols)  
 671 lie clearly above the main sequence of IBs. Two IBs with  $K > 20$  (green thick cross sym-  
 672 bols), though less evident, seem to lie at the bottom envelope of the main IB sequence.  
 673 Finally, IBs with  $K$ -values in 6–10 range appear to lie on the main IB sequence or at a bit  
 674 higher latitudes, as those in Figure 9d.

679 In almost all events in Table 2 latitudinal profiles of the low-altitude fluxes looked  
 680 typical; a gradual increase of the fluxes from the polar boundary toward IB, then the anisotropic  
 681 region where  $0^\circ$ -flux still persists at the level roughly one order of magnitude below  $90^\circ$ -  
 682 flux level before diminishing sharply at  $\sim 55$ – $59^\circ$ . However, the event 2012-07-16/00:24  
 683 (second line in Table 2) was apparently anomalous. The latitudinal profiles of the fluxes  
 684 measured at low altitude for this event are presented in Figure 10. These observations  
 685 were made by NOAA-17 satellite at  $\sim 21$  MLT during the early recovery phase. Fig-

ures 10a and 10b present the precipitated energy fluxes of thermal ( $< 20$  keV) protons and electrons, respectively (measured by TED electrostatic analyzer). Figure 10c shows precipitated (thick) and trapped (thin) proton fluxes in P1 energy channel ( $E > 45$  keV) of MEPED detector. The location of HL IB is marked by the black dashed vertical line. The LL IB (not shown) was defined very close to HL IB for this event. Figure 10d shows precipitated and trapped proton fluxes in P2 channel ( $E > 80$  keV). It can be seen in Figure 10c that there is a region of isotropic precipitations to the equator from IB. The two isotropy regions are separated by anisotropic precipitations (one order of magnitude difference between  $0^\circ$  and  $90^\circ$  fluxes). It can be argued that LL IB should be placed at the equatorial side of the equatormost isotropic precipitations (red dashed line). However, one of the requirements for LL IB selection was that the flux between HL and LL IBs should reveal alternating isotropy (see Section 3.1) but this was not the case for the present event. The equatormost isotropic precipitations of energetic ions ( $E > 45$  keV) coincide with localized precipitations of thermal ions ( $E < 20$  keV, Figure 10a). These features fit the definition of LPEP type 2 structure (Localized Precipitation of Energetic Protons) associated with EMIC waves at plasmopause [Yahnina *et al.*, 2003; Yahnin and Yahnina, 2007]. Interestingly, that the anisotropy region between  $-65^\circ - -61^\circ$  of latitude, so obvious in Figure 10c, can be barely discerned in Figure 10d for the protons with higher energies (P2 channel). Note also that all proton structures are embedded into the electron plasma sheet precipitation (see Figure 10b). The  $K$ -parameter estimated for the IB field line using TS05 was rather small ( $K = 2.4$ ). Figure 9b shows that this IB (blue cross) is located at significantly higher latitude than adjacent IBs. In fact, a few adjacent IBs are located at  $58-60^\circ$ , just where the detached region of isotropic precipitation is seen in Figure 10c. Unfortunately, the adjacent IBs were not in conjunction with THEMIS or there was a large difference between the model field and magnetic measurements and accurate  $K$ -parameter estimate could not be done. Using TS05, we traced the field line from the point of the equatormost boundary of isotropic precipitation (marked by red dashed vertical line in Figure 10c) located at  $-59.4^\circ$  latitude.  $K$ -value of 10.6 was found for the equatorial projection of this field line which is not so much different from  $K = 8$  expected for the FLC-scattering mechanism.

Table 2 shows that two events occurred for approximately the same time on April 24, 2012. For the second event,  $K = 28.8$  was found. Since these two IBs were observed at approximately the same time ( $\sim 6$  min. difference) and approximately the same MLT

( $\sim 1$  h difference), we plot both latitudinal profiles in one figure. Figure 11 shows the observations of two satellites in the same format as Figure 10. The insert between the panels (a) and (b) shows the segments of the orbits. Both satellites crossed the auroral oval from the equator to the pole. The IB was first detected by NOAA-19 at 23.4 MLT and  $\sim 6$  minutes later it was detected by NOAA-18 at 0.2 MLT. It can be seen that the equatorial part of the latitudinal profiles has a similar shape but is displaced by  $\sim 1^\circ$  of latitude. The TS05 model projected one IB to the region with  $K \approx 10$  and another to the region with  $K \approx 29$ .

It is rather difficult to separate spatial and temporal effects in this event. The low-altitude observations can be interpreted as a poleward IB movement or a strong azimuthal dependence (IB at 23 MLT is at  $\sim 1^\circ$  higher latitude in comparison to that at midnight). Note however, that the situation definitely was rather dynamic because the satellites crossed the polar cap boundary at the same MLT but it was displaced by  $\sim 1^\circ$  equatorward for NOAA-18 passage. There were three THEMIS probes in conjunction with low-altitude satellites. The probes were located near the midnight ( $Y_{GSM} = -0.3$ – $-0.2R_E$ ) between  $r = 4R_E$  and  $r = 5.5R_E$  in the region of strong magnetic field ( $B_Z = 60$ – $100$  nT) and strong magnetic field gradient. It is interesting that the TS05 model overestimated  $B_Z$  at the innermost probe position and underestimated it at two outer probes. That means that  $B_Z^{OBS} - B_Z^{MOD}$  is negative for innermost probe and positive for outer probes. That is, the model overestimates the  $B_Z$  gradient. When  $\Delta B_Z$  is computed using Equation 5, the contributions from different probes partly cancel each other out. If  $\Delta B_Z$  were computed with absolute values of the sum members,  $\Delta B_Z$  values would be 6.9 and 4.5 nT for NOAA-19 and NOAA-18, respectively. In such a case, the IB with  $K = 28.8$  (NOAA-19) would not pass our criterion for the 5 nT model agreement with the measurements. In addition, MLT conjunction between THEMIS probes and low-altitude satellite is worse for NOAA-19 IB ( $\sim 1$  h difference in MLT).

#### 4 Discussion

Our study was initially motivated by two reasons. One was an expectation that during magnetic storms, the generally enhanced level of wave activity plays an increasing role in proton precipitation and, possibly, in the formation of the proton isotropic boundary (IB). Another reason was the recently raised doubts about the role of FLC-scattering as a dominant mechanism of IB formation, particularly, a large percentage of high  $K$ -parameter

754 values found at the equatorial end of the IB field line, whereas the  $K \sim 8$  was expected in  
755 case of the FLC-related mechanism [Sergeev *et al.*, 2015b; Ilie *et al.*, 2015]. It should be  
756 noted that both papers used the models in the same way like we use in our study, but they  
757 had a small number (only a few dozen) events at their disposal.

758 Studying the IB-related  $K$ -values in  $\sim 2000$  events, we have found that, although the  
759 distribution is rather broad, it is centered not far from the theoretical estimate ( $median(K) <$   
760  $13$  in all plots of Figure 4). Moreover, we found that the points with  $K$  values inside 4.5–  
761  $13$  interval are located in the narrow region within  $1R_E$  from the  $K = 8$  location as dic-  
762 tated by strong radial  $B$ -gradients in the quasi-dipole magnetic field. Such events con-  
763 stitute a large part of all events, being more than a third of all events in the uncorrected  
764  $K$ -distribution (Figure 4) and about a half in the corrected  $K$ -distribution (Figure 7).

765 For a smaller subset of events ( $\sim 250$ ), we were also able to control independently  
766 the accuracy of model predictions by comparing them to magnetic observations at the  
767 THEMIS probes approximately-conjugated with low-altitude IBs. Like in previous sim-  
768 ilar comparisons based on geostationary spacecraft and IB observations [Donovan *et al.*,  
769 2003a], we found a very clear correlation between  $\Delta B_Z$  and the  $K$  parameter estimations  
770 (Figure 6). Using this dependence, the  $K$  values were tentatively corrected to take into ac-  
771 count the model deviations from the actual magnetic field observations. We use asterisk  
772 symbol to differentiate the corrected  $K^*$  value from original uncorrected  $K$  value. After  
773 being corrected,  $K^*$  distribution was centered at  $K^* \sim 10$  (Figure 7). This is not as ter-  
774 ribly different from the corrected average value of  $K^* \sim 17$  (for 30 keV proton IB) and  
775  $K^* \sim 13$  (for 80 keV proton IB) found by Sergeev *et al.* [2015b], but it is very far from  
776 median value  $K \sim 33$  of Ilie *et al.* [2015]. We remind that global MHD model was used  
777 for mapping in the latter paper. It should be noted that a good agreement of the modeled  
778 and observed  $B_Z$  does not fully guarantee an accurate estimation of  $K$ -parameter because  
779 Equation 1 also includes  $dB_X/dZ$  in the denominator. Unfortunately, multi-spacecraft con-  
780 figurations allowing the estimation of  $dB_X/dZ$  in the current sheet center at the proper  
781 range of radial distance occur quite rarely. We emphasize that sufficient statistics and ap-  
782 propriate tools allowing to exclude a systematic bias in model predictions are both very  
783 essential in this kind of studies, and in our paper, we attempted to improve in both as-  
784 pects.

785 Another effect of the correction was that the  $K^*$ -distribution also became more nar-  
786 row, especially at large  $K^*$  values, the percentage of events with  $K^* > 30$  was reduced to  
787 5%, twice as small compared to those found before the correction (Figure 4). The demon-  
788 stration that large width of  $K$ -distributions comes mainly from inaccurate model predic-  
789 tions is another important conclusion of our study. This is consistent with findings by  
790 *Sergeev et al.* [2015b] who used a more sophisticated model adapted to the data of the  
791 THEMIS spacecraft cluster, and found that samples with  $K > 32$  occurred only in the  
792 dataset in which the spacecraft distance from the IB field line was greater than  $2R_E$  (a  
793 very rigorous requirement). The existence of large scatter into the lower  $K$ - region is one  
794 more argument in favor of model inaccuracies as a basic origin of strong scatter in  $K$ -  
795 space: the pitch-angle scattering amplitude is known to grow exponentially with decreas-  
796 ing  $K$  so the pitch-angle scattering amplitude is normally  $\sim 10$  times larger at  $K \sim 4$  than  
797 at  $K \sim 8$  [*Delcourt et al.*, 1996].

798 To a large extent, the inaccurate  $B$ -field representation should be the main origin of  
799 large  $K^*$ -scatter which still remains after the correction was applied. This is especially  
800 obvious during active conditions when the magnetic configuration can be drastically differ-  
801 ent at nearby locations (say, inside and outside of the plasma bubbles/BBFs), when large  
802 temporal variations occur (see an example in Figure 11 and rapid variations of the IB lat-  
803 itude in Figure 9) and when the  $B$ -field values and its gradients inevitably deviate from  
804 their smooth representation in the average empirical models. At the same time, the theo-  
805 retical threshold of strong scatter can also vary depending on the unusual steep radial  $B_Z$ -  
806 gradients, etc. Its very large changes were demonstrated in current sheet geometries for  
807 different transverse distributions of electric current density [*Delcourt et al.*, 1996, 2006]  
808 or even for additional guide component ( $B_Y$ ) of the magnetic field [*Delcourt et al.*, 2000].  
809 It should be noted that the analytical functions, defining a geometry of the current sheet  
810 in the empirical models, are rather simple and, in fact, are not necessarily physically self-  
811 consistent with thermal plasma [*Zaharia and Cheng*, 2003]. Some efforts toward devel-  
812 oping a plasma-magnetic field consistent magnetospheric model and using it for studying  
813 pitch-angle scattering mechanism were recently made [see *Yue et al.*, 2014, and references  
814 therein] but, at present, this model still lacks a flexibility in the representation of different  
815 states of the magnetospheric activity. The actual range of possible  $K$ -threshold variations  
816 for  $\sim 30$ – $80$  keV proton IB still remains unspecified, and this definitely requires future  
817 studies.

818 There are another two important results indicating that wave-particle interaction  
819 plays a minor role, if any, in the IB formation. First, we found no appreciable dependence  
820 of the  $K^*$ -parameter distribution on MLT whereas the IB latitude reveals rather clear de-  
821 pendence in Figure 2. However, if the waves played an essential role, such dependence  
822 would be expected because occurrences of the EMIC waves [Halford *et al.*, 2010; Us-  
823 anova *et al.*, 2012] and anomalous IB dispersion [Dubyaagin *et al.*, 2013] both reveal strong  
824 dependence on MLT. On the other hand, it might be speculated that negative result was  
825 due to a limited number of events  $\sim 250$  or/and because the IBs on the dusk flank (15–  
826 21 MLT) were not considered. Second, the  $K^*$ -parameters estimations do not reveal vis-  
827 ible dependence on the IB latitude, except for events with IB located at extremely low or  
828 high latitudes ( $< 59^\circ$  or  $> 66^\circ$ ), for which the  $K$ -parameter correction could fail. The find-  
829 ings imply that the FLC-scattering is a persistent mechanism of IB formation operating in  
830 a variety of magnetospheric conditions.

831 An additional contribution to large  $K$ -scattering may also come from the uncertainty  
832 in the IB identification itself, and this is what we also addressed in our study. We found  
833 that the uncertainty of IB selection is highly critical for  $\sim 10\%$  of events. However, even  
834 uncertainty as small as  $\sim 0.5^\circ$ , found for  $\sim 15\%$  of events, can lead to a significant un-  
835 certainty in estimated  $K$  values. Although it does not affect the main statistical results of  
836 our study, it can be of key importance for case studies (as demonstrated in Figure 10).  
837 The problem of the IB identification during storm activity deserves to be addressed in the  
838 future studies, possibly, using supportive information from other detectors/telescopes.

839 Although our results clearly emphasize the dominant role of FLC-scattering for  
840 IB formation, still two indications can be interpreted as rare manifestations of the wave-  
841 particle interaction in the IB vicinity. The first indication is high  $K$  values found for IB  
842 latitude lower than  $\sim 59^\circ$ . Since the wave-related precipitations were observed mostly at  
843 low-latitudes [Yahnin and Yahnina, 2007], these IB could be formed by wave-particle in-  
844 teraction process. Less than 10% of IBs are located at latitude lower than  $59^\circ$  but they are  
845 of special interest because they all correspond to SYM-H\* minimum period (Figure 2).  
846 Second, we discovered a specific class of events, when the empirical formula (Equation 2)  
847 describing the IB latitude variation with SYM-H and  $P_{dyn}$  fails to predict the IB location  
848 but instead predicts the location of the equatorial cut-off of the moderately anisotropic  
849 precipitation in the loss-cone, mapped to the region of high  $K$ -parameter (see Figure 3).  
850 For these events, the real IBs are located at significantly higher latitudes. The latitudinal

851 profiles of the  $0^\circ$ - and  $90^\circ$ -fluxes closely remind those for the specific events investigated  
852 by [Gvozdevsky *et al.*, 1997] and called Low-Latitude Proton Precipitation (LLPP). The  
853 most plausible mechanism explaining the moderately anisotropic precipitations between  
854 the observed and predicted IBs is a moderate scattering by the electromagnetic waves.  
855 It is very puzzling why, in some cases, Equation 2, which was obtained using the large  
856 dataset of IBs mostly formed by FLC-scattering, predicts the location of some specific  
857 boundary formed by wave-particle interaction process. As a possible explanation, it can be  
858 speculated that the wave-related IBs constitute a larger part of all IBs than it seems from  
859 the analysis of  $K$ -distribution. However, not willing to speculate on this topic further, we  
860 leave this puzzle to future research. The estimate for occurrence rate of the wave-related  
861 IBs can be also found as a percentage of events with  $K > 13$  in Figure 7, which is 30%–  
862 40%.

## 863 5 Conclusions

864 Using a large dataset of the low-altitude Isotropic Boundary (IB) observations (~2000 IB  
865 determinations during nine geomagnetic storms), we used the TS05 model to estimate the  
866 adiabaticity parameter  $K$  (ratio of the magnetic field line curvature radius to the particle  
867 gyroradius) at the equatorial part of the IB field line during nine moderate geomagnetic  
868 storms. The concurrent magnetic field measurements onboard THEMIS probes in the  
869 equatorial magnetotail were used to control the TS05 deviations from the real magnetic  
870 configuration. It was found that the TS05 configuration is systematically understretched  
871 during the intervals of an SYM-H minimum and this leads to  $K$ -parameter overestima-  
872 tion. For small group of events with THEMIS data available, we introduced a tentative  
873  $K$ -parameter correction which compensates the model bias based on  $B_Z$  difference be-  
874 tween model prediction and THEMIS observation. This correction resulted in a significant  
875 reduction of the statistical scatter in the corrected  $K^*$ -parameter distribution, demonstrating  
876 the importance of the independent control of the model accuracy for this kind of studies.  
877 Contrary to the findings of *Sergeev et al.* [2015b] and *Ilie et al.* [2015], we found the me-  
878 dian  $K$ -parameter value of 9–12 being close to  $K = 8$  expected for the field-line-curvature  
879 scattering (FLC-scattering) mechanism of IB formation. Numerical tests with the TS05  
880 model showed that  $K$  values in 4.5–13 interval correspond to the points located within  
881  $1R_E$  from the  $K=8$  field line, correspondingly, we consider the  $K < 13$  values as those in-  
882 dicating the FLC mechanism. Different estimates give percentages of such events between

883 60% and 80%. The remaining 20%–40% provide an upper estimate for the occurrence of  
884 IBs formed by the wave-particle interaction process. Finally, we did not find any apprecia-  
885 ble dependence of the  $K$ -parameter distribution on MLT whereas the IB latitude reveals  
886 rather clear MLT asymmetry. Although the IB latitude undergoes dramatic variations dur-  
887 ing storm-time, the  $K$ -parameter distribution also does not show a clear dependence on the  
888 IB latitude, except for events with IB located at extremely low latitudes ( $< 59^\circ$ ). Summa-  
889 rizing our findings we conclude that the pitch-angle scattering on the curved field lines is  
890 a dominant mechanism of the energetic proton isotropic boundary formation operating in a  
891 variety of magnetospheric conditions.

### 892 **A: NOAA/POES proton MEPED Detector Calibrations**

893 The proton SEM-2 MEPED detector measures fluxes in a few energy channels (P1,  
894 P2, P3, . . .). There are two solid-state telescopes for each of energy channels. One tele-  
895 scope points to local zenith (it is referred to as  $0^\circ$ -telescope) and another points along the  
896 satellite orbit (referred to as  $90^\circ$ -telescope). At auroral latitudes, the  $0^\circ$ - telescope detects  
897 ion fluxes precipitating into a loss-cone. The  $90^\circ$ - telescope detects fluxes of the locally  
898 trapped ions. The proton MEPED detector is subjected to degradation which leads to an  
899 increase of the low energy threshold [Asikainen *et al.*, 2012; Sandanger *et al.*, 2015; Øde-  
900 gaard *et al.*, 2016]. The shift of the low energy threshold is described using the calibra-  
901 tion factor  $\alpha$  so that  $E_{corrected} = \alpha \cdot E_{nominal}$ . Asikainen *et al.* [2012] provided the  $\alpha$  val-  
902 ues up to the year 2011. Sandanger *et al.* [2015] used different method and provided the  $\alpha$   
903 values for later years (not for all satellites). There is some (moderate) discrepancy between  
904 the  $\alpha$  values obtained in these two works. Taking into account all these results, we use the  
905  $\alpha$  values as given in Table A.1 to estimate the low energy limit for P1 proton  $0^\circ$  detector.  
906 However, the  $90^\circ$ -telescope is subjected to even stronger degradation. It means that its low  
907 energy limit is even higher than that for  $0^\circ$  detector.

910 Generally, a recomputation of the fluxes to the nominal energy range requires the in-  
911 formation about the spectrum [Asikainen *et al.*, 2012] and, in any case, this procedure is  
912 rather complex. Instead of doing this, we use the P1  $0^\circ$  -telescope flux without any cor-  
913 rection (just assuming that the flux corresponds to the energy of the channel estimated  
914 using  $\alpha$ -factors). However, since  $E_{corrected}$  is different for  $0^\circ$ - and  $90^\circ$ -telescopes, the  $90^\circ$   
915 flux must be scaled to the  $0^\circ$ -telescope energy range. The algorithm of such scaling was  
916 developed in DUBYAGIN *et al.* [2013], however, it worked well only for certain oval cross-



908 **Table A.1.**  $\alpha$ -values for the 0°-telescope for P1 energy channel. The satellite index is specified in the top  
 909 row.

Year \ Sat.	01	02	15	16	17	18	19
2011	1.0	1.09	2.16	1.53	1.47	1.01	1.00
2012	1.0	1.12	2.20	1.57	1.51	1.04	1.03
2013	1.0	1.13	2.22	1.59	1.53	1.05	1.04

917 ings. The possible reason for the poor algorithm performance can be a contamination of  
 918 the MEPED data by energetic neutral atoms (ENA) from ring current regions (a level of  
 919 contamination is different for inbound and outbound oval crossings) [Søråas *et al.*, 2003;  
 920 Søråas and Sorbo, 2013b]. In addition, the detector also responds to heavier ions (See  
 921 Section 4 of Søråas *et al.* [2002] for more details), which are ubiquitous during storms.  
 922 For this reason, we develop a simplified approach. We determine correction separately for  
 923 every auroral oval crossing. It is assumed that correction for 90° flux can be represented  
 924 as a constant multiplier. We search for such multiplier that the resulting 90°-flux fits the  
 925 0°-flux in the region where the isotropy is expected. This region was defined as a region  
 926 poleward from the maximum of the 0°-flux (so called b2i-boundary [Newell *et al.* , 1996]).  
 927 The 90°-flux calibration factor was computed as a *median*(flux0/flux90) in the isotropy  
 928 region.

### 929 Acknowledgments

930 The NOAA/POES particle data were downloaded form National Geophysical Data Center  
 931 website: <https://www.ngdc.noaa.gov/stp/satellite/poes/index.html>. THEMIS magnetic field  
 932 data were loaded and calibrated using official software at <http://themis.ssl.berkeley.edu>.  
 933 The solar wind and IMF data were downloaded from the OMNI database from the GSFC/SPDF  
 934 OMNIWeb interface at <http://omniweb.gsfc.nasa.gov>. The 1-min. resolution SYM-H and  
 935 AE, AL indices were provided by the World Data Center for geomagnetism, Kyoto ([http://wdc.kugi.kyoto-  
 936 u.ac.jp/](http://wdc.kugi.kyoto-u.ac.jp/)). The precomputed input parameters for *Tsyganenko and Sitnov* [2005] model were  
 937 downloaded from <http://geo.phys.spbu.ru/~tsyganenko/modeling.html>. The part of the re-  
 938 search done by N. Ganushkina and S. Dubyagin has received funding from the European  
 939 Union Seventh Framework Programme (FP7/20072013) under grant agreement 606716  
 940 SPACESTORM and from the European Union Horizon 2020 Research and Innovation

941 programme under grant agreement 637302 PROGRESS. N. Ganushkina thanks the In-  
942 ternational Space Science Institute in Bern, Switzerland, for their support of the interna-  
943 tional teams on “Analysis of Cluster Inner Magnetosphere Campaign data, in application  
944 the dynamics of waves and wave-particle interaction within the outer radiation belt” and  
945 “Ring current modeling: Uncommon Assumptions and Common Misconceptions”. Sup-  
946 port for N. Ganushkina at the University of Michigan was provided by NASA research  
947 grants NNX14AF34G, NNX17AI48G, NNX17AB87G, 80NSSC17K0015.

## 948 **References**

- 949 Angelopoulos, V. (2008a), The THEMIS mission, *Space Sci. Rev.*, *141*, 5–34,  
950 doi:10.1007/s11214-008-9336-1.
- 951 Auster, H. U., et al. (2008), The THEMIS fluxgate magnetometer, *Space Sci. Rev.*, *141*,  
952 235–236, doi: 10.1007/s11214-008-9365-9.
- 953 Asikainen, T., V. Maliniemi, and K. Mursula, Modeling the contributions of ring, tail,  
954 and magnetopause currents to the corrected Dst index, *J. Geophys. Res.*, *115*, A12203,  
955 doi:10.1029/2010JA015774, 2010
- 956 Asikainen, T., K. Mursula, and V. Maliniemi, Correction of detector noise and recal-  
957 ibration of NOAA/MEPED energetic proton fluxes, *J. Geophys. Res.*, *117*, A09204,  
958 doi:10.1029/2012JA017593, 2012
- 959 Baker, K. B., and S. Wing (1989), A new magnetic coordinate system for  
960 conjugate studies at high latitudes, *J. Geophys. Res.*, *94*(A7), 9139–9143,  
961 doi:10.1029/JA094iA07p09139.
- 962 Burton, R. K., R. L. McPherron, and C. T. Russell (1975), An empirical relationship  
963 between interplanetary conditions and Dst, *J. Geophys. Res.*, *80*(31), 4204–4214,  
964 doi:10.1029/JA080i031p04204.
- 965 Büchner, J., and L. M. Zelenyi (1989), Regular and chaotic charged particle motion in  
966 magnetotail-like field reversals: 1. Basic theory of trapped motion, *J. Geophys. Res.*,  
967 *94*(A9), 11821–11842, doi:10.1029/JA094iA09p11821.
- 968 Delcourt, D. C., J.-A. Sauvaud, R. F. Martin Jr., and T. E. Moore (1996), On the nonadia-  
969 batic precipitation of ions from the near-Earth plasma sheet, *J. Geophys. Res.*, *101*(A8),  
970 17409–17418, doi:10.1029/96JA01006.
- 971 Delcourt, D. C., L. M. Zelenyi, and J.-A. Sauvaud (2000), Magnetic moment scattering  
972 in a field reversal with nonzero BY component, *J. Geophys. Res.*, *105*(A1), 349–359,

973 doi:10.1029/1999JA900451.

974 Delcourt, D. C., H. V. Malova, and L. M. Zelenyi (2006), Quasi-adiabaticity in bifurcated  
975 current sheets, *Geophys. Res. Lett.*, *33*, L06106, doi:10.1029/2005GL025463.

976 Donovan, E. F., B. J. Jackel, I. Voronkov, T. Sotirelis, F. Creutzberg, and N. A. Nicholson  
977 (2003a), Ground-based optical determination of the b2i boundary: A basis for an optical  
978 MT-index, *J. Geophys. Res.*, *108*, 1115, doi:10.1029/2001JA009198, A3.

979 Donovan, E., B. Jackel, D. Klumpar, and R. Strangeway (2003b), Energy dependence of  
980 the isotropy boundary latitude, in *Proc. of Atmos. Studies by Optical Methods*, vol. 92,  
981 pp. 11–14, Sodankylä Geophysical Observatory Publications, Finland.

982 Dubyagin, S., Ganushkina, N., Apatenkov, S., Kubyshkina, M., Singer, H., and Liemohn,  
983 M.: Geometry of duskside equatorial current during magnetic storm main phase as de-  
984 duced from magnetospheric and low-altitude observations, *Ann. Geophys.*, *31*, 395–408,  
985 doi:10.5194/angeo-31-395-2013, 2013.

986 Erlandson, R. E., and A. J. Ukhorskiy (2001), Observations of electromagnetic ion cy-  
987 clotron waves during geomagnetic storms: Wave occurrence and pitch angle scattering,  
988 *J. Geophys. Res.*, *106*(A3), 3883–3895, doi:10.1029/2000JA000083.

989 Evans, D. S., and M. S. Greer, Polar orbiting environmental satellite space environment  
990 monitor: 2. Instrument descriptions and archive data documentation, *NOAA Tech.*  
991 *Memo.*, OAR SEC-93, NOAA, Boulder, Colo, 2000

992 Fraser, B.J., and T.S. Nguyen (2001), Is the plasmopause a preferred source region of  
993 electromagnetic ion cyclotron waves in the magnetosphere?, *Journal of Atmospheric and*  
994 *Solar-Terrestrial Physics*, *63*, 11, 1225–1247

995 Ganushkina, N. Yu., Pulkkinen, T. I., Kubyshkina, M. V., Sergeev, V. A., Lvova, E. A.,  
996 Yahnina, T. A., Yahnin, A. G., and Fritz, T.: Proton isotropy boundaries as measured on  
997 mid- and low-altitude satellites, *Ann. Geophys.*, *23*, 1839–1847, doi:10.5194/angeo-23-  
998 1839-2005, 2005.

999 Gary, S. P., M. F. Thomsen, L. Yin, and D. Winske (1995), Electromagnetic proton  
1000 cyclotron instability: Interactions with magnetospheric protons, *J. Geophys. Res.*,  
1001 *100*(A11), 21961–21972, doi:10.1029/95JA01403.

1002 Gilson, M. L., J. Raeder, E. Donovan, Y. S. Ge, and L. Kepko (2012), Global simulation  
1003 of proton precipitation due to field line curvature during substorms, *J. Geophys. Res.*,  
1004 *117*, A05216, doi:10.1029/2012JA017562.

- 1005 Gvozdevsky, B. B., V. A. Sergeev, and K. Mursula (1997), Long lasting energetic proton  
1006 precipitation in the inner magnetosphere after substorms, *J. Geophys. Res.*, *102(A11)*,  
1007 24333–24338, doi:10.1029/97JA02062.
- 1008 Halford, A. J., B. J. Fraser, and S. K. Morley, EMIC wave activity during geomag-  
1009 netic storm and nonstorm periods: CRRES results, *J. Geophys. Res.*, *115*, A12248,  
1010 doi:10.1029/2010JA015716, 2010
- 1011 Hauge R., and F. Søråas (1975), Precipitation of > 115 keV protons in the evening and  
1012 forenoon sectors in relation to the magnetic activity, *Planetary and Space Science*, *23*, 8,  
1013 1141–1154.
- 1014 Horne, R. B., and R. M. Thorne (1993), On the preferred source location for the con-  
1015 vective amplification of ion cyclotron waves, *J. Geophys. Res.*, *98(A6)*, 9233–9247,  
1016 doi:10.1029/92JA02972.
- 1017 Ilie, R., N. Ganushkina, G. Toth, S. Dubyagin, and M. W. Liemohn (2015), Test-  
1018 ing the magnetotail configuration based on observations of low-altitude isotropic  
1019 boundaries during quiet times, *J. Geophys. Res. Space Physics*, *120*, 10,557–10,573,  
1020 doi:10.1002/2015JA021858.
- 1021 Imhof, W. L., J. B. Reagan, and E. E. Gaines (1977), Fine-scale spatial structure in the  
1022 pitch angle distributions of energetic particles near the midnight trapping boundary, *J.*  
1023 *Geophys. Res.*, *82(32)*, 5215–5221, doi:10.1029/JA082i032p05215.
- 1024 Imhof, W., J. Reagan, and E. Gaines (1979), Studies of the sharply defined L depen-  
1025 dent energy threshold for isotropy at the midnight trapping boundary, *J. Geophys. Res.*,  
1026 *84(A11)*, 6371–6384, doi:10.1029/JA084iA11p06371.
- 1027 Keika, K., K. Takahashi, A. Y. Ukhorskiy, and Y. Miyoshi (2013), Global characteristics  
1028 of electromagnetic ion cyclotron waves: Occurrence rate and its storm dependence, *J.*  
1029 *Geophys. Res. Space Physics*, *118*, 4135–4150, doi:10.1002/jgra.50385.
- 1030 Kennel, C. F., and H. E. Petschek (1966), Limit on stably trapped particle fluxes, *J. Geo-*  
1031 *phys. Res.*, *71(1)*, 1–28, doi:10.1029/JZ071i001p00001.
- 1032 Kozyra, J. U., T. E. Cravens, A. F. Nagy, E. G. Fontheim, and R. S. B. Ong  
1033 (1984), Effects of energetic heavy ions on electromagnetic ion cyclotron wave  
1034 generation in the plasmopause region, *J. Geophys. Res.*, *89(A4)*, 2217–2233,  
1035 doi:10.1029/JA089iA04p02217.
- 1036 Kubyshkina, M. V., V. A. Sergeev, and T. I. Pulkkinen (1999), Hybrid Input Algorithm:  
1037 An event-oriented magnetospheric model, *J. Geophys. Res.*, *104(A11)*, 24977–24993,

1038 doi:10.1029/1999JA900222.

1039 Liang, J., E. Donovan, B. Ni, C. Yue, F. Jiang, and V. Angelopoulos (2014), On an  
1040 energy-latitude dispersion pattern of ion precipitation potentially associated with  
1041 magnetospheric EMIC waves, *J. Geophys. Res. Space Physics*, *119*, 8137–8160,  
1042 doi:10.1002/2014JA020226.

1043 Lvova, E. A., Sergeev, V. A., and Bagautdinova, G. R.: Statistical study of the proton  
1044 isotropy boundary, *Ann. Geophys.*, *23*, 1311–1316, doi:10.5194/angeo-23-1311-2005,  
1045 2005.

1046 Newell, P. T., Y. I. Feldstein, Y. I. Galperin, and C.-I. Meng (1996), Morphology of night-  
1047 side precipitation, *J. Geophys. Res.*, *101*(A5), 10737–10748, doi:10.1029/95JA03516.

1048 Ødegaard, L.-K., G. H. Nesse Tyssoy, M. I. Sandanger, J. Stadsnes, and F. Søråas (2016),  
1049 Space Weather impact on the degradation of energetic proton detectors, *J. Space*  
1050 *Weather Space Clim.*, doi:10.1051/swsc/2016020.

1051 Pulkkinen, T. I., D. N. Baker, R. J. Pellinen, J. BÄijchner, H. E. J. Koskinen, R. E. Lopez,  
1052 R. L. Dyson, and L. A. Frank (1992), Particle scattering and current sheet stability  
1053 in the geomagnetic tail during the substorm growth phase, *J. Geophys. Res.*, *97*(A12),  
1054 19283–19297, doi:10.1029/92JA01189.

1055 Sandanger, M. I., L.-K. G. Ødegaard, H. Nesse Tyssøy, J. Stadsnes, F. Søråas, K. Ok-  
1056 savik, and K. Aarsnes (2015), In-flight calibration of NOAA POES proton detectors-  
1057 Derivation of the MEPED correction factors, *J. Geophys. Res. Space Physics*, *120*,  
1058 9578–9593, doi:10.1002/2015JA021388.

1059 Sergeev, V. A., Sazhina, E. M., Tsyganenko, N. A., Lundblad, J. A., Søråas, F., Pitch-angle  
1060 scattering of energetic protons in the magnetotail current sheet as the dominant source  
1061 of their isotropic precipitation into the nightside ionosphere, *Planetary and Space Sci-*  
1062 *ence*, *31*, 1147–1155., 1983

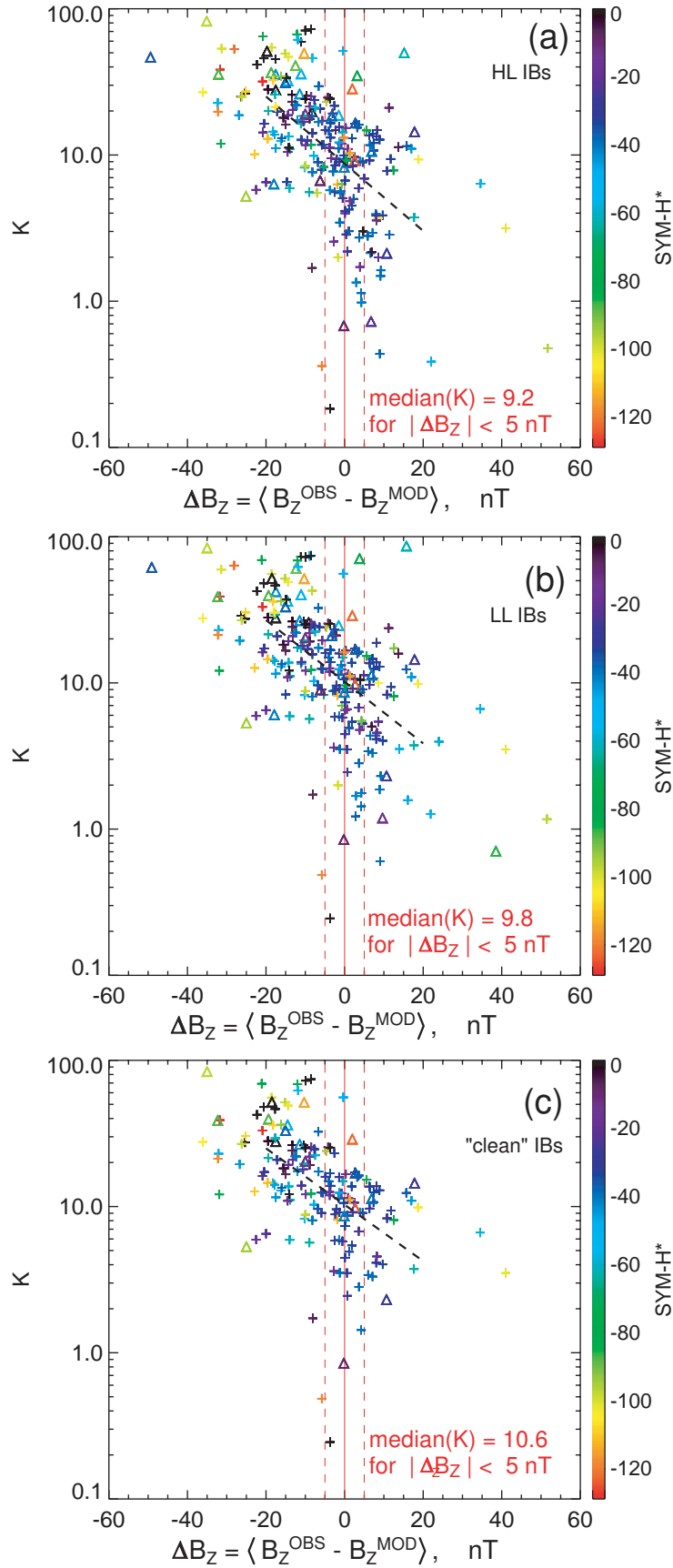
1063 Sergeev, V. A., M. Malkov, and K. Mursula (1993), Testing the isotropic boundary algo-  
1064 rithm method to evaluate the magnetic field configuration in the tail, *J. Geophys. Res.*,  
1065 *98*(A5), 7609–7620, doi:10.1029/92JA02587.

1066 Sergeev, V. A., Chernyaeva, S. A., Apatenkov, S. V., Ganushkina, N. Y., and Dubyagin,  
1067 S. V.: Energy-latitude dispersion patterns near the isotropy boundaries of energetic pro-  
1068 tons, *Ann. Geophys.*, *33*, 1059–1070, doi:10.5194/angeo-33-1059-2015, 2015a.

1069 Sergeev, V. A., Chernyaev, I. A., Angelopoulos, V., and Ganushkina, N. Y.: Magneto-  
1070 spheric conditions near the equatorial footpoints of proton isotropy boundaries, *Ann.*

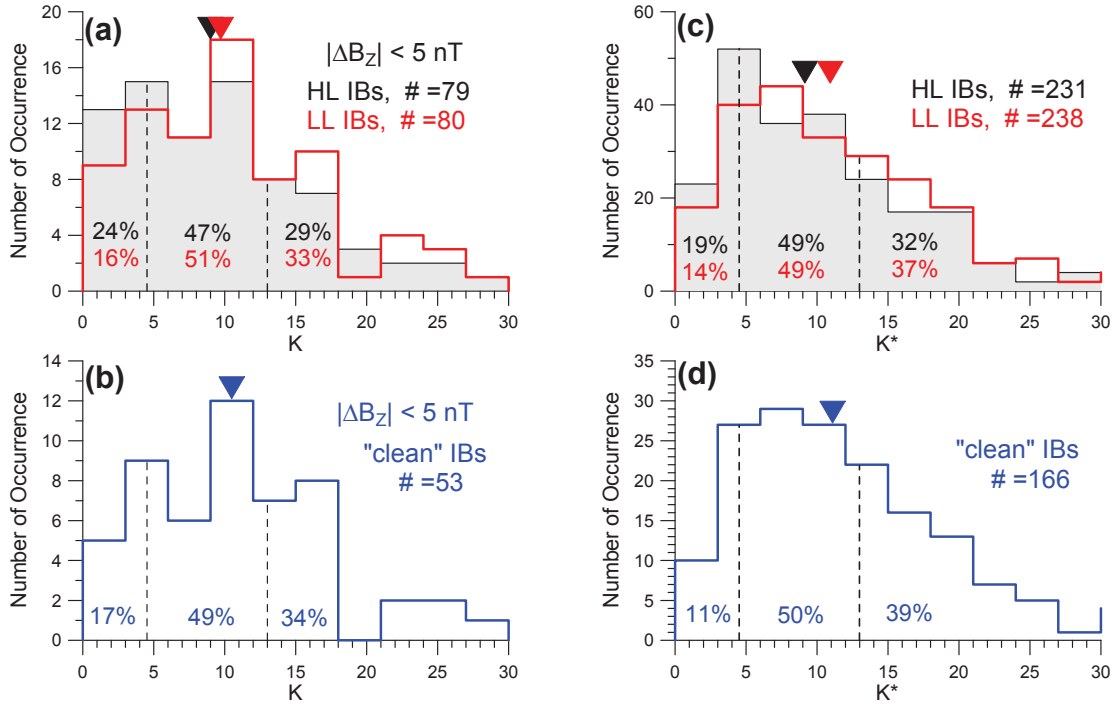
- 1071 *Geophys.*, 33, 1485–1493, doi:10.5194/angeo-33-1485-2015, 2015b.
- 1072 Søråas, F., J. Å Lundblad, B. Hultqvist, On the energy dependence of the ring current pro-  
1073 ton precipitation, *Planet. Space Sci.*, 25, 757–763, 1977.
- 1074 Søråas, F., K. Aarsnes, K. Oksavik, and D. S. Evans, Ring current intensity es-  
1075 timated from low-altitude proton observations, *J. Geophys. Res.*, 107(A7),  
1076 doi:10.1029/2001JA000123, 2002.
- 1077 Søråas, F., K. Oksavik, K. Aarsnes, D. S. Evans, and M. S. Greer (2003), Storm  
1078 time equatorial belt – an "image" of RC behavior, *Geophys. Res. Lett.*, 30, 1052,  
1079 doi:10.1029/2002GL015636, 2.
- 1080 Søråas, F., K. M. Laundal, and M. Usanova (2013a), Coincident particle and optical ob-  
1081 servations of nightside subauroral proton precipitation, *J. Geophys. Res. Space Physics*,  
1082 118, 1112–1122, doi:10.1002/jgra.50172.
- 1083 Søråas, F., and M. Sorbo (2013b), Low altitude observations of ENA from the  
1084 ring current and from the proton oval, *J. Atmos. Sol. Terr. Phys.*, 99, 104–110,  
1085 doi:10.1016/j.jastp.2012.10.003.
- 1086 Tsyganenko, N. A., and M. I. Sitnov (2005), Modeling the dynamics of the inner  
1087 magnetosphere during strong geomagnetic storms, *J. Geophys. Res.*, 110, A03208,  
1088 doi:10.1029/2004JA010798.
- 1089 Usanova, M. E., I. R. Mann, J. Bortnik, L. Shao, and V. Angelopoulos (2012), THEMIS  
1090 observations of electromagnetic ion cyclotron wave occurrence: Dependence on  
1091 AE, SYMH, and solar wind dynamic pressure, *J. Geophys. Res.*, 117, A10218,  
1092 doi:10.1029/2012JA018049.
- 1093 Usanova, M. E., Mann, I. R. and Darrouzet, F. (2016) EMIC Waves in the Inner Magne-  
1094 tosphere, in *Low-Frequency Waves in Space Plasmas* (eds A. Keiling, D.-H. Lee and V.  
1095 Nakariakov), *John Wiley & Sons, Inc, Hoboken, NJ*. doi:10.1002/9781119055006.ch5
- 1096 Wang, C.-P., S. G. Zaharia, L. R. Lyons, and V. Angelopoulos (2013), Spatial distributions  
1097 of ion pitch angle anisotropy in the near-Earth magnetosphere and tail plasma sheet, *J.*  
1098 *Geophys. Res. Space Physics*, 118, 244–255, doi:10.1029/2012JA018275.
- 1099 Xiong, Y., Yuan, Z., and Wang, J.: Energetic ions scattered into the loss cone with obser-  
1100 vations of the Cluster satellite, *Ann. Geophys.*, 34, 249–257, doi:10.5194/angeo-34-249-  
1101 2016, 2016.
- 1102 Yahnina, T. A., Yahnin, A. G., Kangas, J., Manninen, J., Evans, D. S., Demekhov, A. G.,  
1103 Trakhtengerts, V. Yu., Thomsen, M. F., Reeves, G. D., and Gvozdevsky, B. B.: Ener-

- 1104       getic particle counterparts for geomagnetic pulsations of Pc1 and IPDP types, *Ann. Geo-*  
1105       *phys.*, 21, 2281–2292, doi:10.5194/angeo-21-2281-2003, 2003.
- 1106       Yahnin, A. G., and T. A. Yahnina (2007), Energetic proton precipitation related to ion-  
1107       cyclotron waves, *J. Atmos. Sol. Terr. Phys.*, 69, 1690–1706.
- 1108       Yuan, Z., Y. Xiong, D. Wang, M. Li, X. Deng, A. G. Yahnin, T. Raita, and J. Wang  
1109       (2012), Characteristics of precipitating energetic ions/electrons associated with the  
1110       wave-particle interaction in the plasmaspheric plume, *J. Geophys. Res.*, 117, A08324,  
1111       doi:10.1029/2012JA017783.
- 1112       Yue, C., C.-P. Wang, L. Lyons, J. Liang, E. F. Donovan, S. G. Zaharia, and M. Hender-  
1113       son (2014), Current sheet scattering and ion isotropic boundary under 3-D empiri-  
1114       cal force-balanced magnetic field, *J. Geophys. Res. Space Physics*, 119, 8202–8211,  
1115       doi:10.1002/2014JA020172.
- 1116       Zaharia, S., and C. Z. Cheng (2003), Can an isotropic plasma pressure distribu-  
1117       tion be in force balance with the T96 model field? *J. Geophys. Res.*, 108, 1412,  
1118       doi:10.1029/2002JA009501, A11.

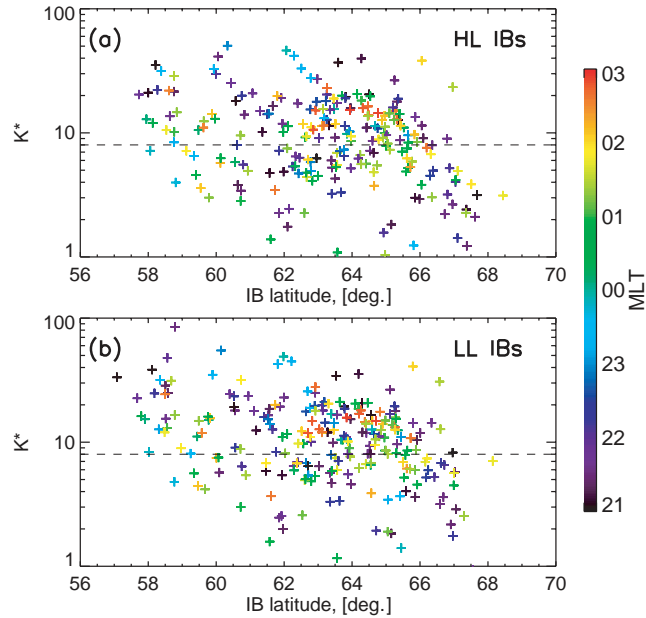


533 **Figure 6.** K-parameter versus the model  $B_z$  error. Triangles and cross symbols correspond to main and re-  
 534 recovery phases, respectively. K-parameter estimations are made for HL IBs (a) and LL IBs (b) and “clean” IBs  
 535 (c).  
 This article is protected by copyright. All rights reserved.

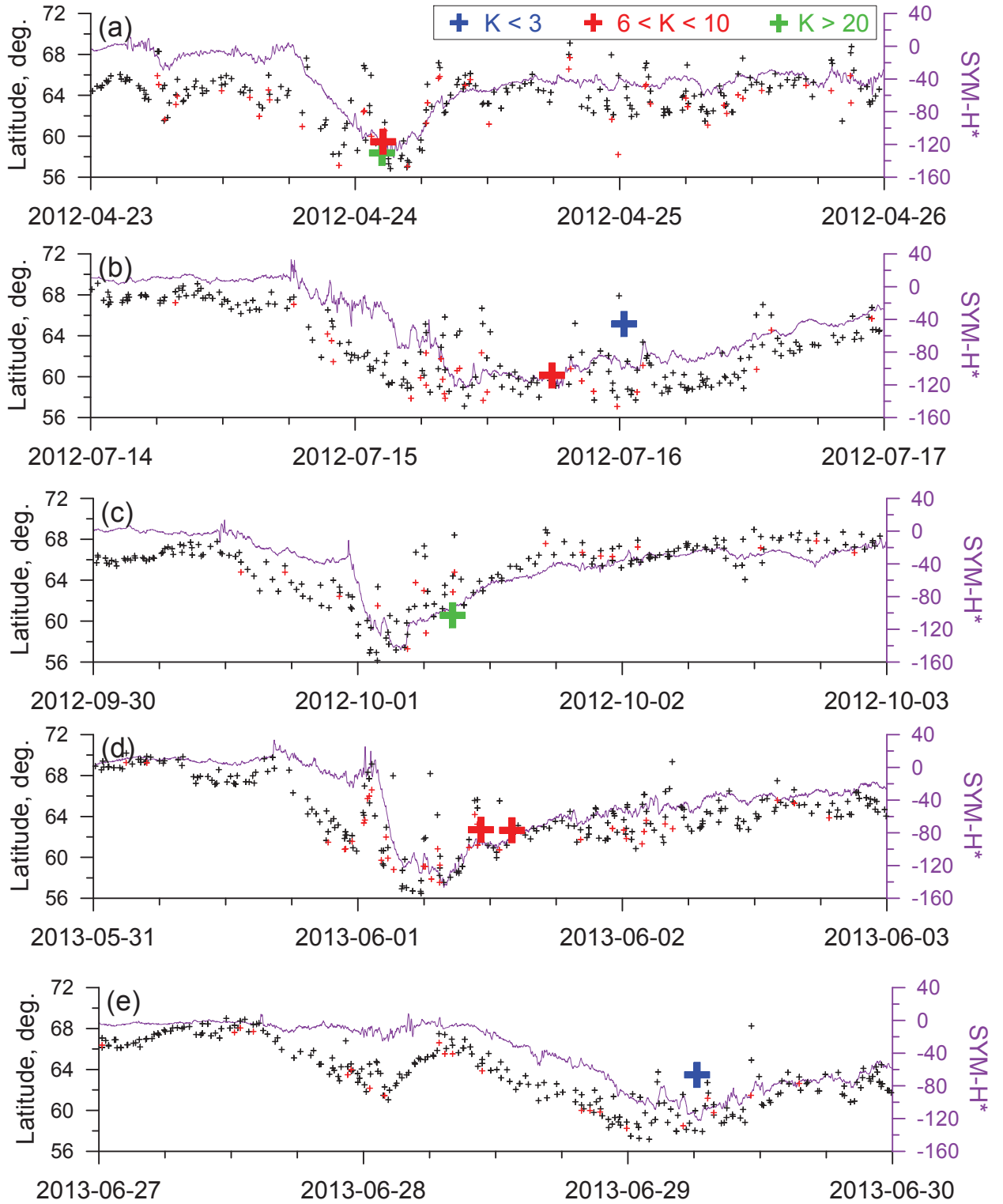




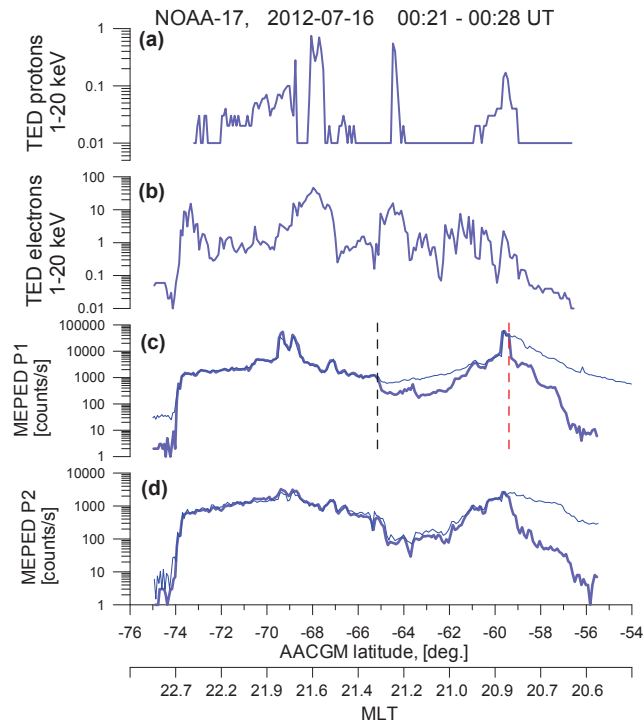
547 **Figure 7.** Panels (a) and (b): the histograms of  $K$ -parameter for events with  $|\Delta B_z| < 5$  nT. Panels (c) and  
 548 (d): and histograms of  $K$ -parameter mathematically shifted to  $\Delta B_z = 0$  line. The format is the same as in Fig-  
 549 ure 4.



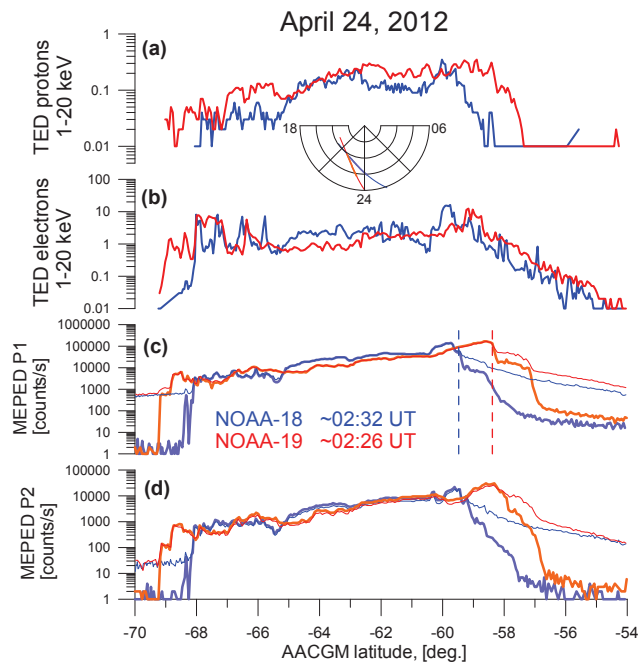
597 **Figure 8.** Corrected  $K$ -values versus absolute value of IB latitude for HL (a) and LL (b) datasets. Dashed  
 598 lines mark  $K = 8$  level. Color shows IB MLT.



664 **Figure 9.** The SYM-H\* (magenta curve) with the overlapped latitude of observed HL and LL IB (absolute  
 665 value, black and red crosses, respectively). Thick colored crosses correspond to the IB latitudes for events  
 666 listed in Table 2 (see text).



675 **Figure 10.** The latitudinal profiles of the observed parameters. (a) integrated proton energy flux ( $E = 1-$   
 676  $20$  keV), (b) electron energy flux ( $E = 1-20$  keV), (c) integrated proton number fluxes ( $E > 45$  keV), (d) inte-  
 677 grated proton number fluxes ( $E > 80$  keV). Black dashed vertical line marks the IB position. Red dashed ver-  
 678 tical line marks the equatorward IB (see text)



727 **Figure 11.** The latitudinal profiles of the observed parameters for two consecutive auroral oval crossings  
 728 separated by ~6 minutes. NOAA-18 and -19 observations are shown in blue and red color, respectively. The  
 729 insert between (a) and (b) panels shows the segments of the orbits.

Figure 1.

Author Manuscript

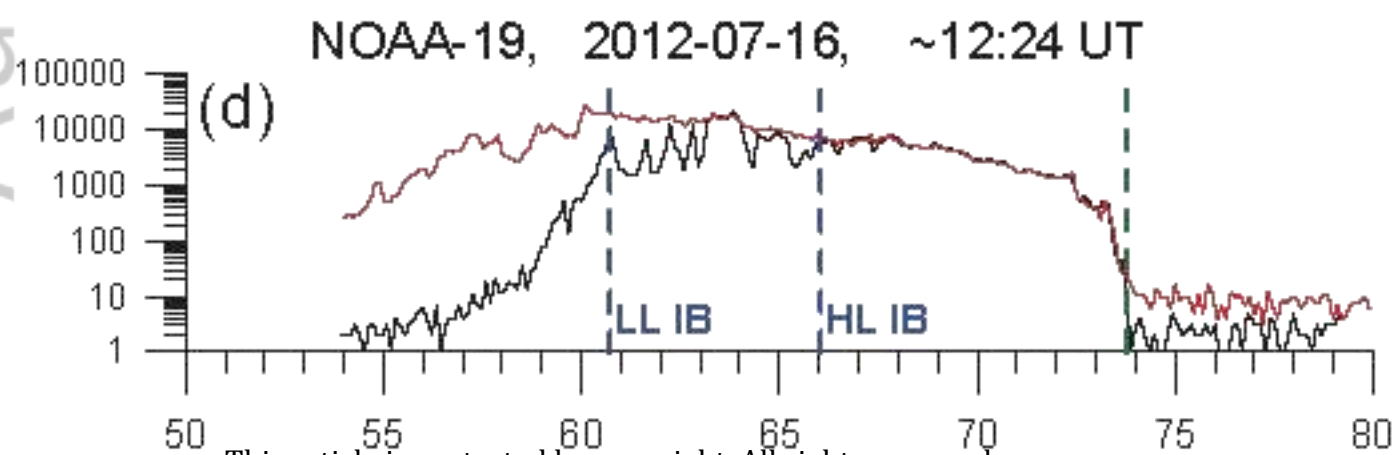
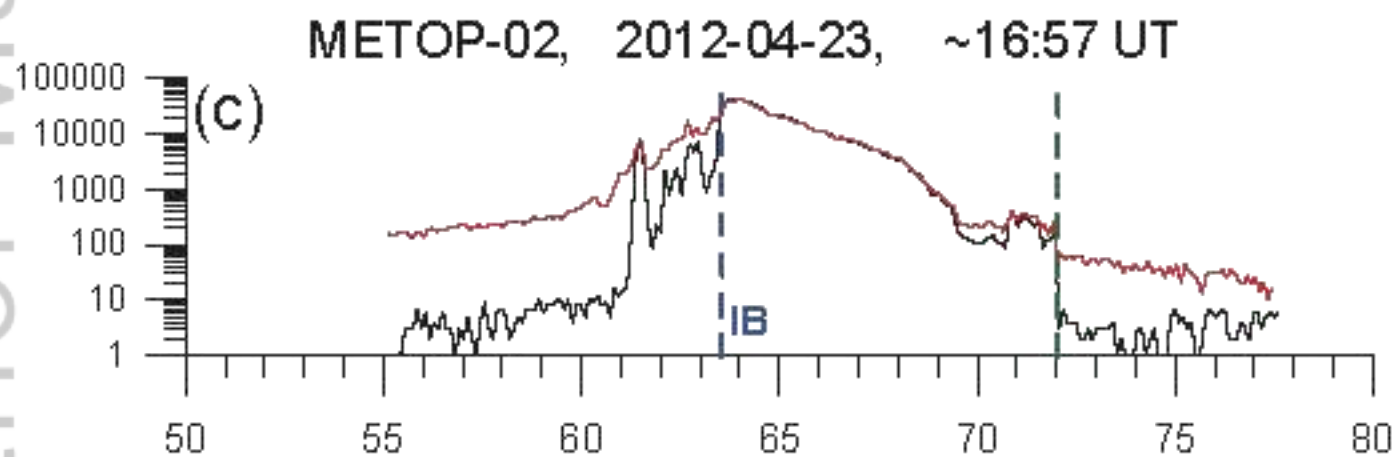
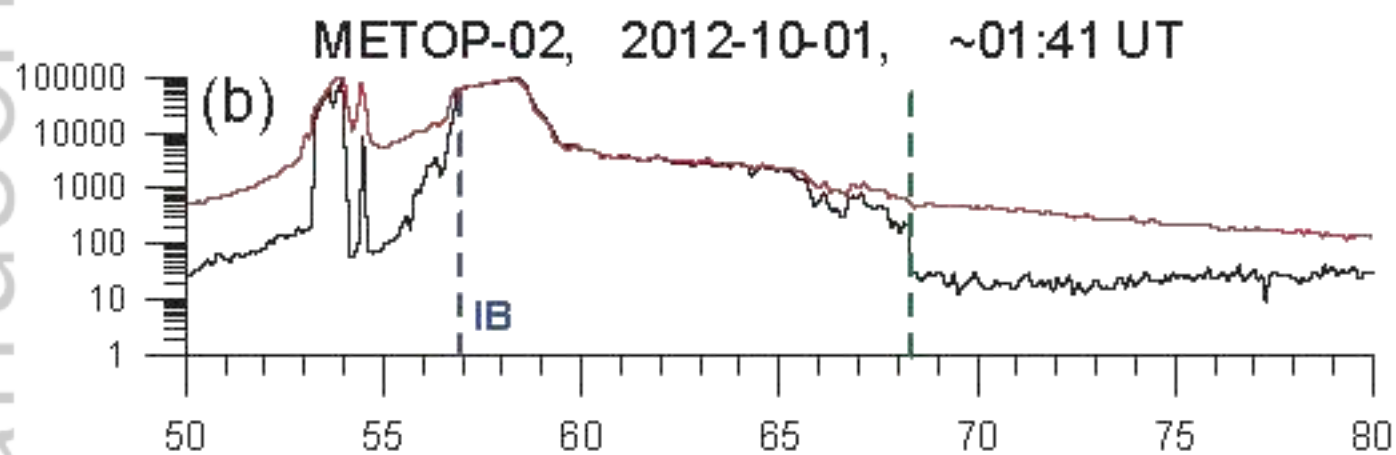
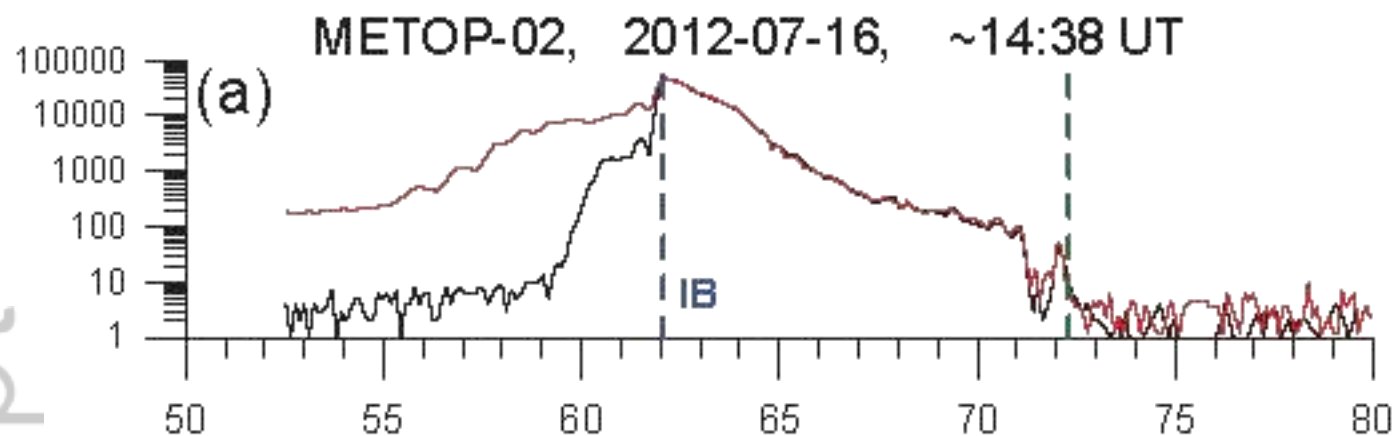
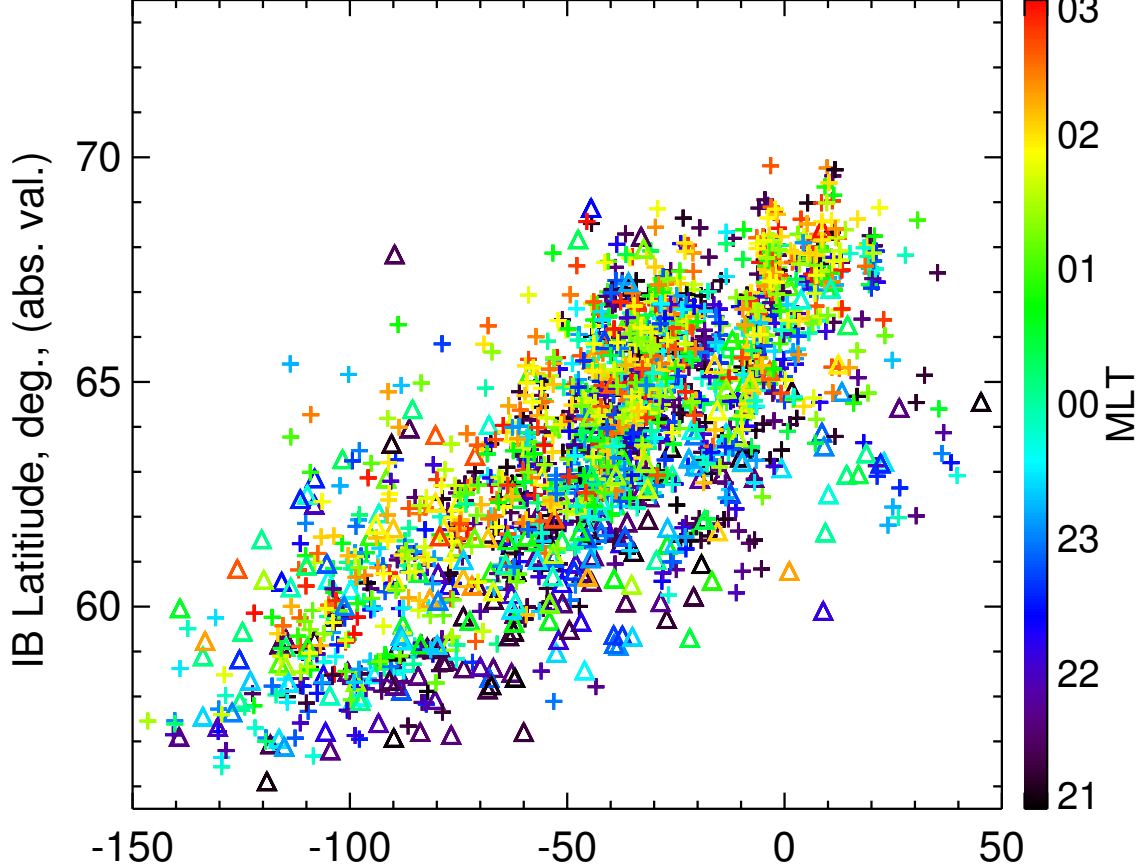


Figure 2.

Author Manuscript



This article is protected by copyright. All rights reserved.



Figure 3.

Author Manuscript

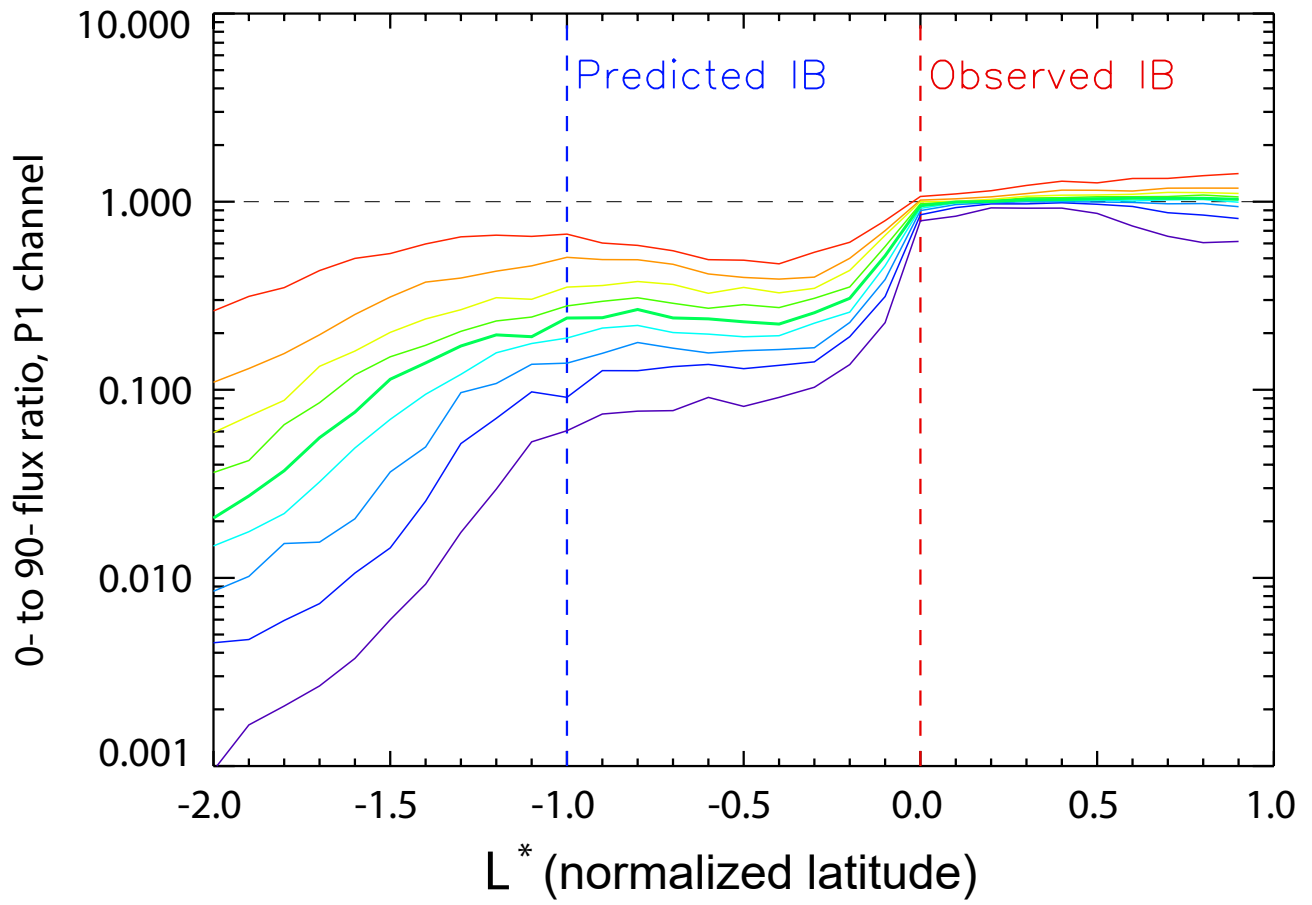


Figure 4.

Author Manuscript

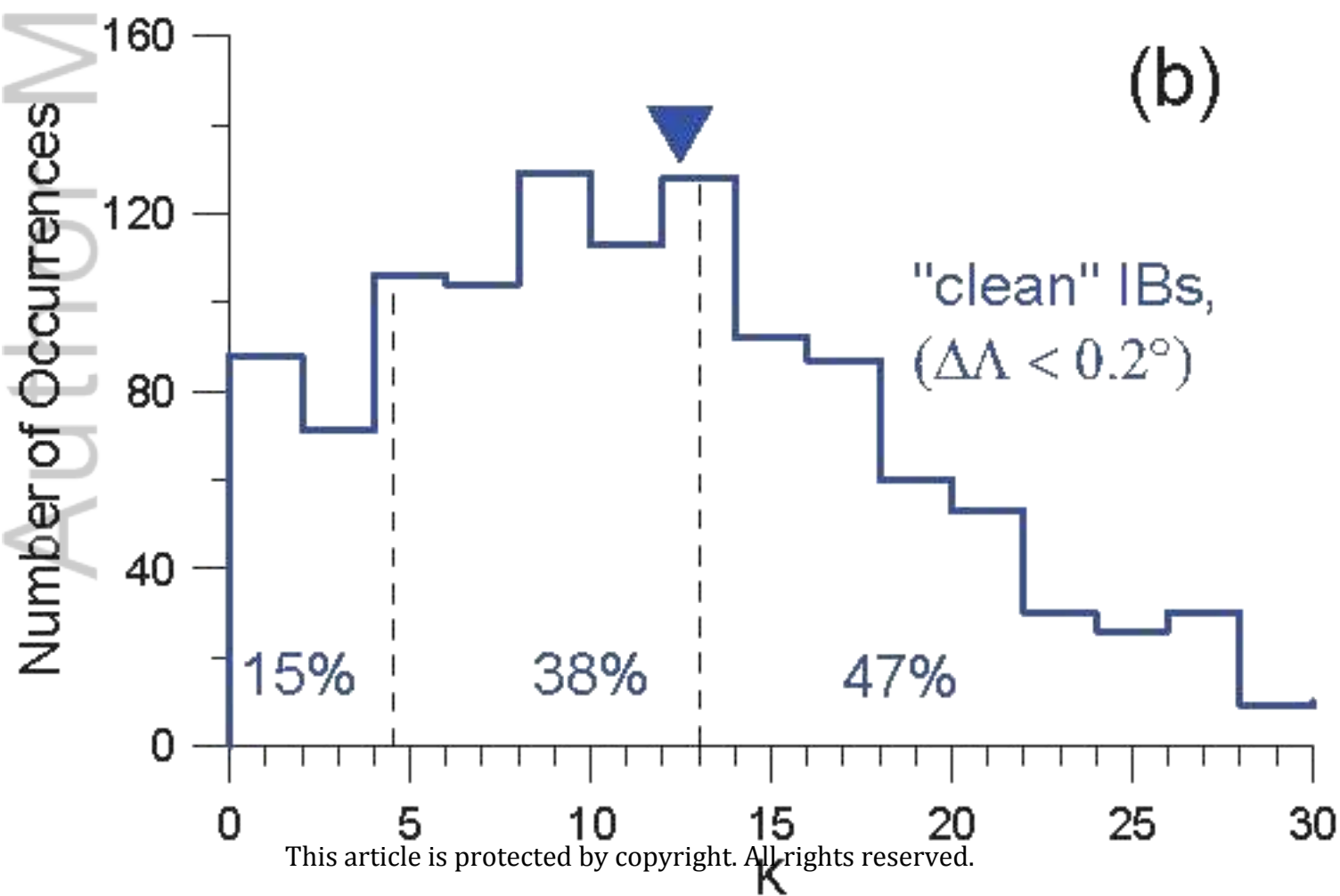
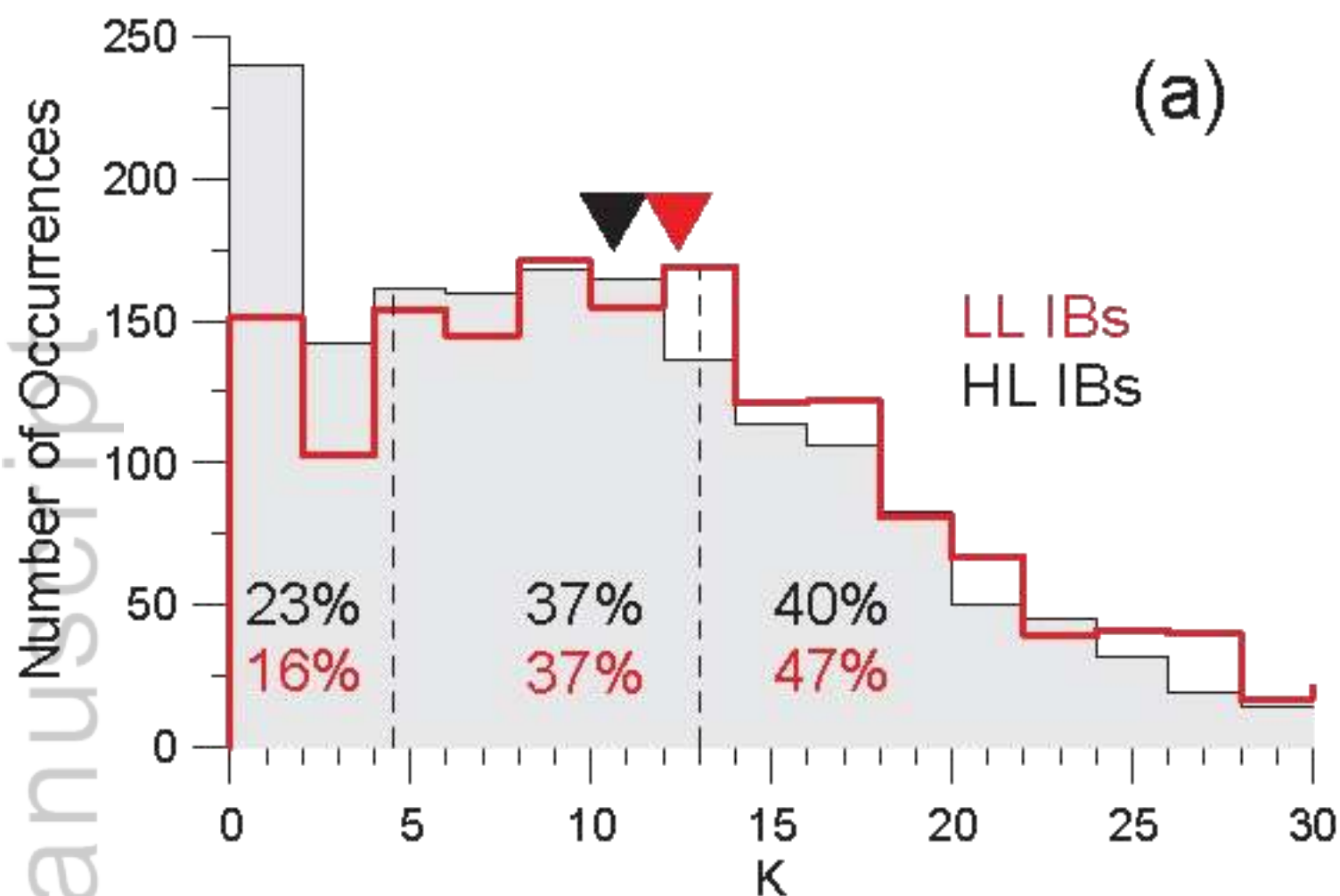


Figure 5.

Author Manuscript

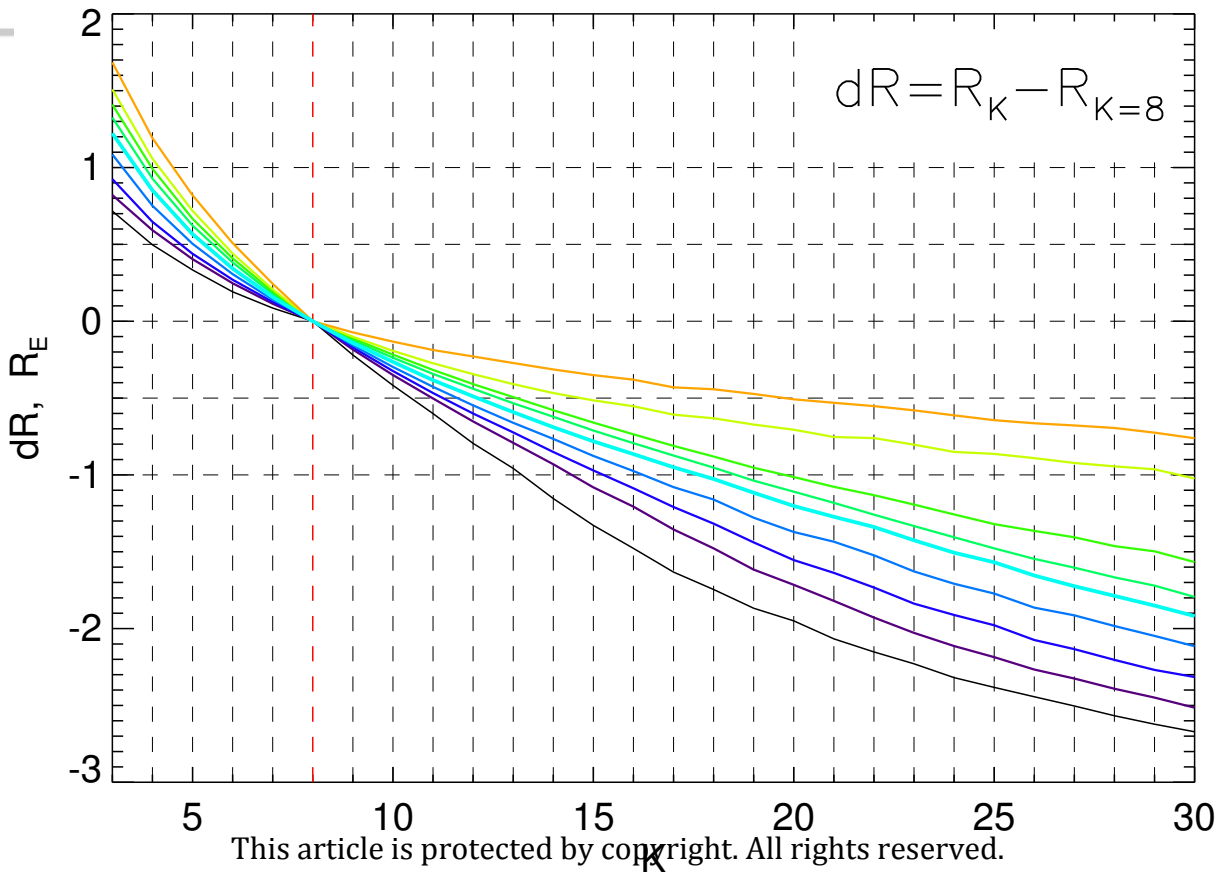


Figure 6.

Author Manuscript

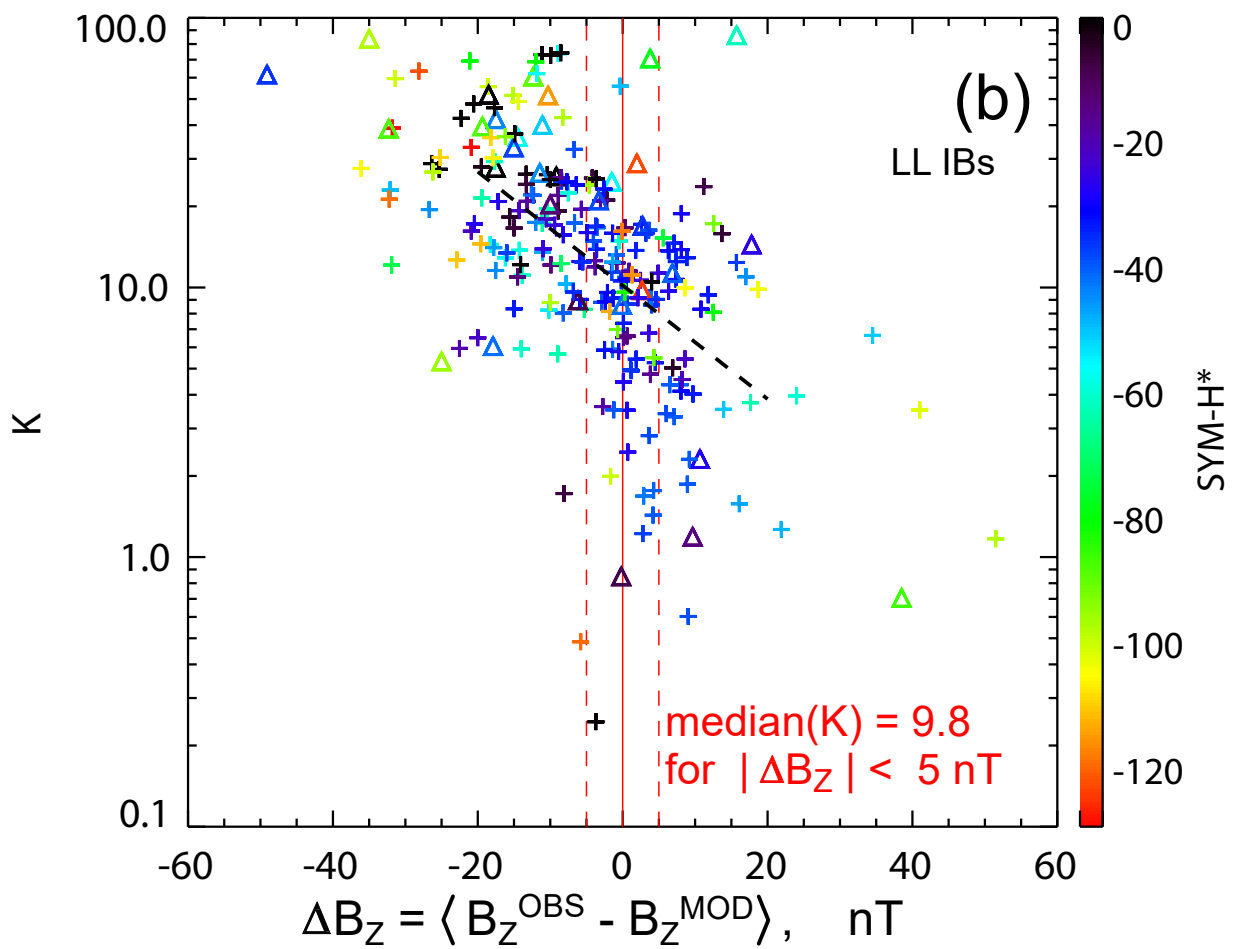
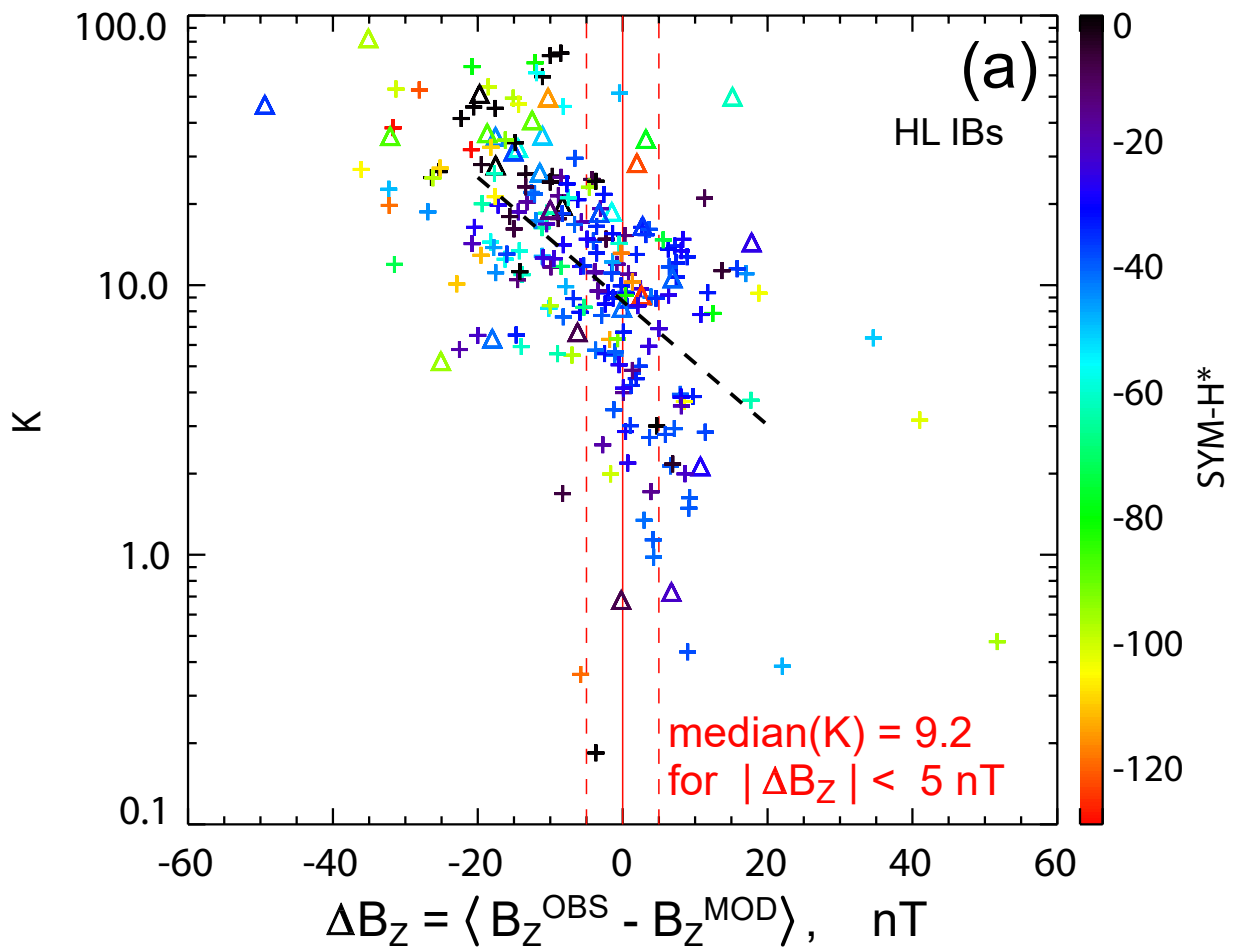




Figure 7.

Author Manuscript

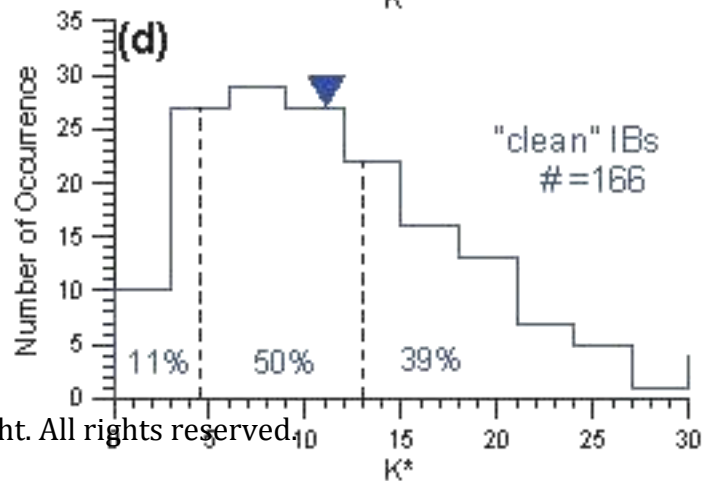
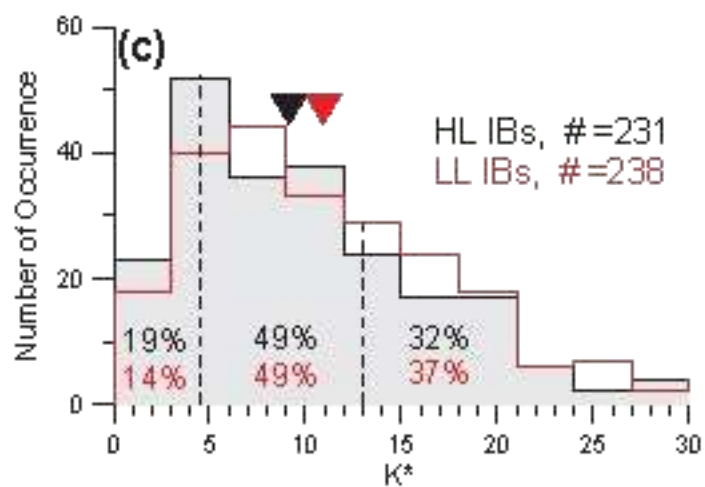
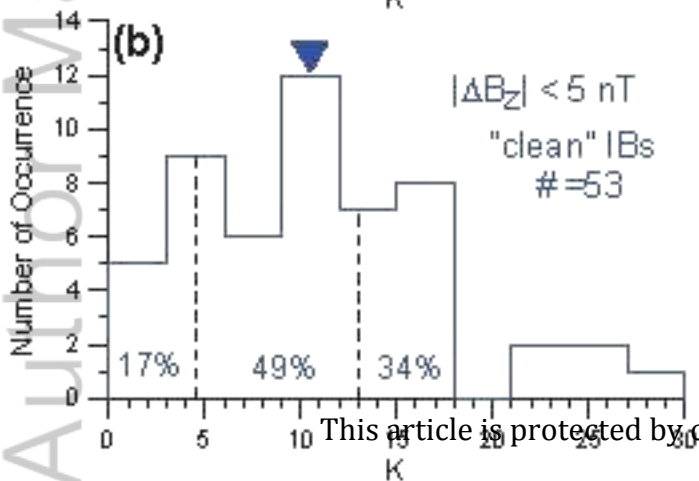
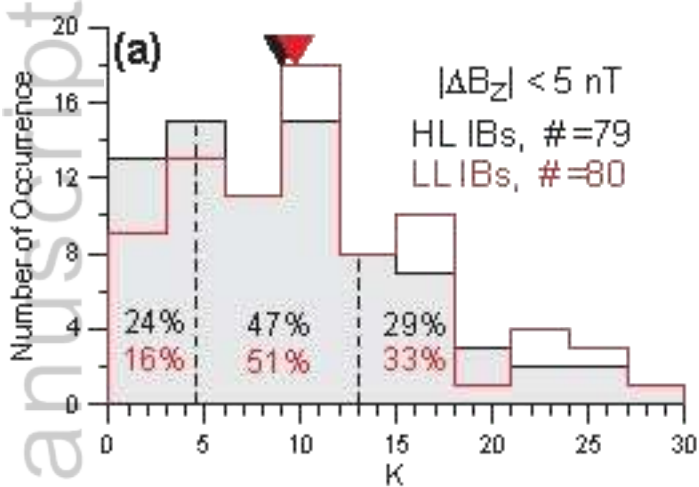


Figure 8.

Author Manuscript

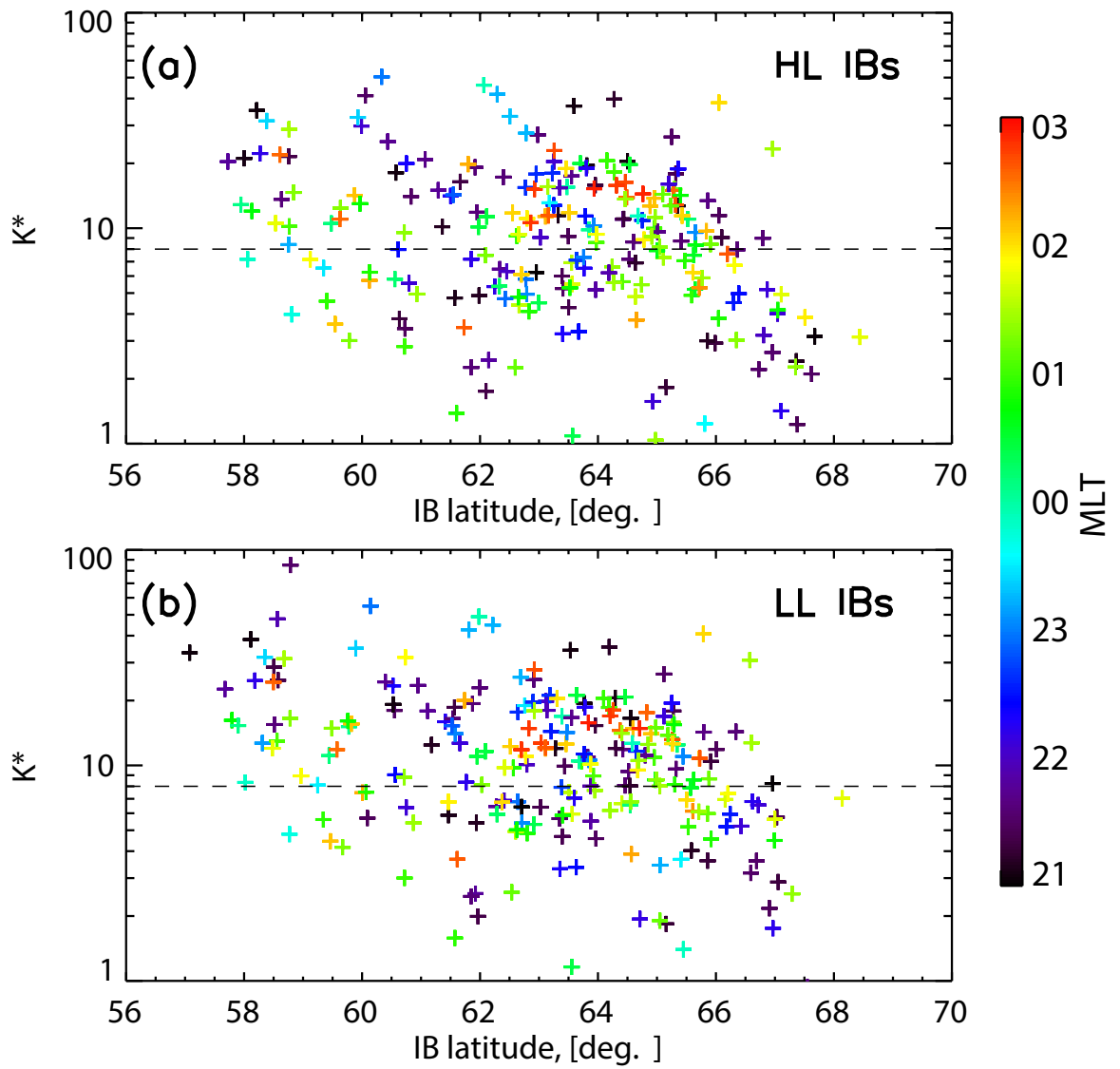


Figure 9.

Author Manuscript

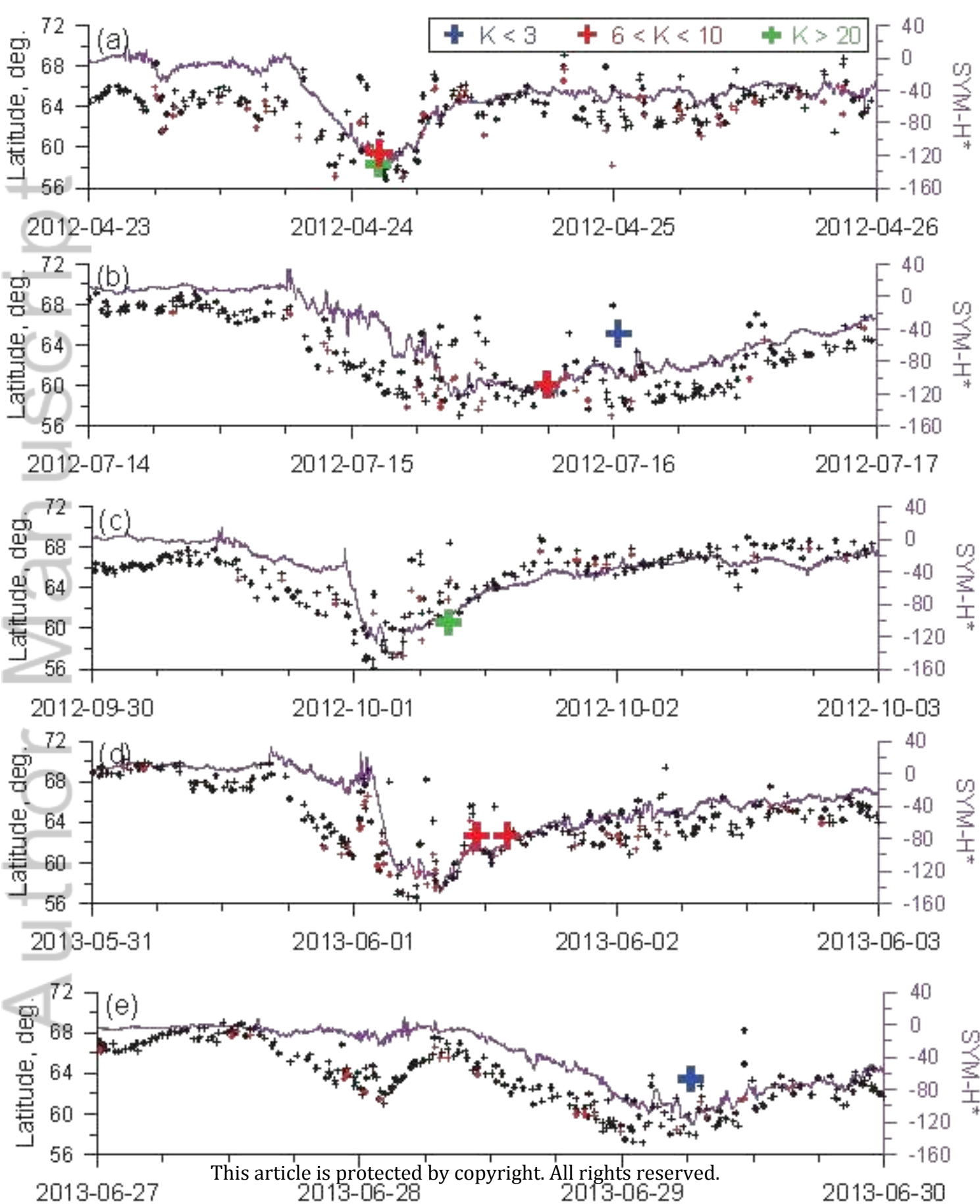
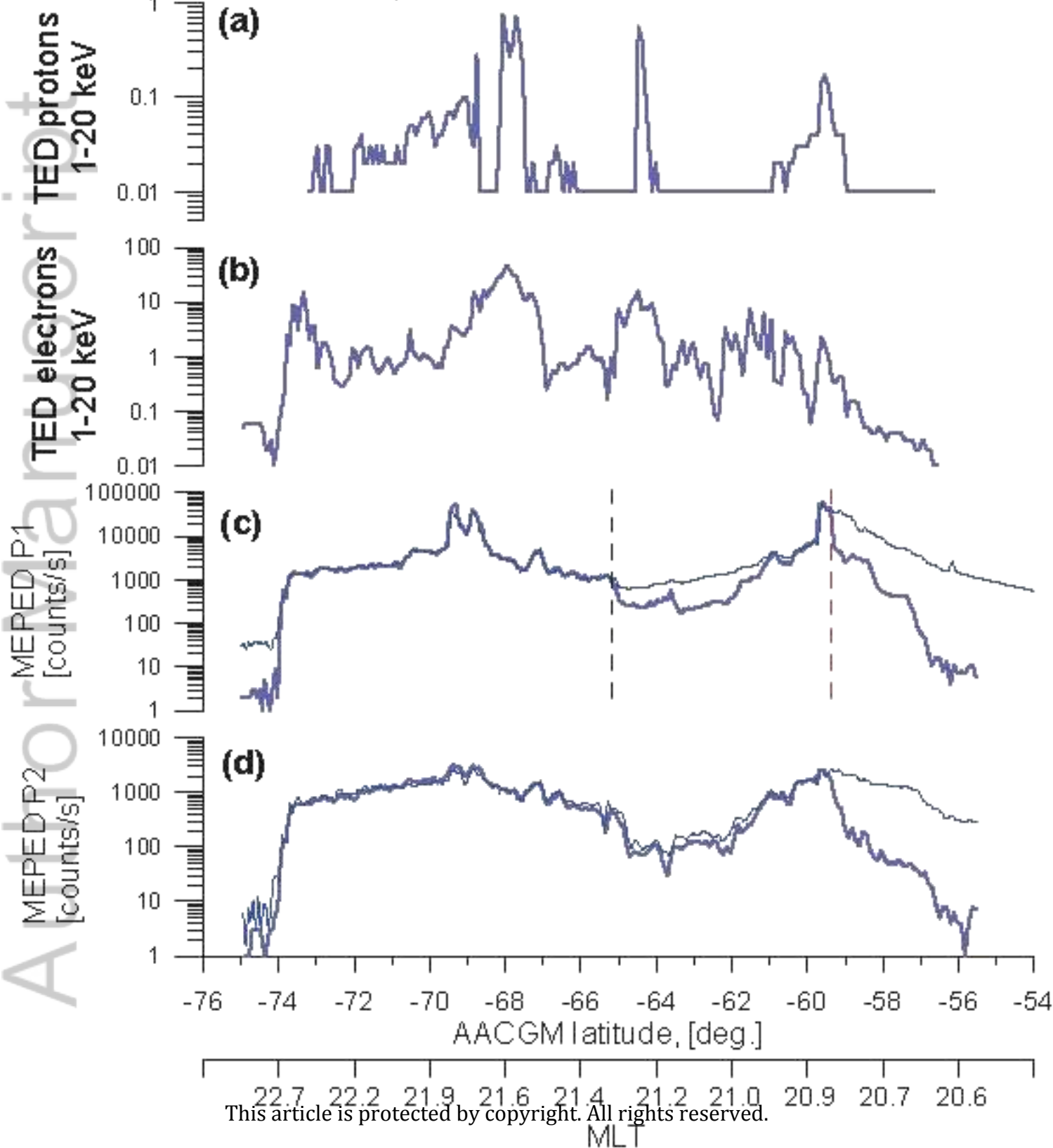


Figure 10.

Author Manuscript

NOAA-17, 2012-07-16 00:21 - 00:28 UT



This article is protected by copyright. All rights reserved.

MLT



Figure 11.

Author Manuscript

April 24, 2012

